(1:5,000; Biosource International), washed again, and then developed using a chemiluminescent ECL kit (Amersham Pharmacia Biotech).

Videomicroscopy

For time-lapse imaging, cells were plated on no. 1 1/2 coverslips. The coverslips were mounted in an opened rose chamber covered by a membrane permeable to CO_2. The microscope stage was equipped with a device enabling regulation of temperature and CO_2 level. Time-lapse Z sequences were collected on a Leica DMIRBE microscope controlled by Metamorph software (Universal Imaging Corp.). This microscope was equipped with a motorized stage, a 100× 1.4 NA Plan Apo Lens, and a cooled CCD camera (MicroMax 5 MHz; Roper Scientific). The final magnification on the camera chip was 134 nm/pixel (using the 2 × 2 binning mode of the camera). The illumination device was a 100-W halogen lamp with the potentiometer set under 8V to avoid overillumination. The acquisition time was 400 milliseconds. As a rule, 6–10 sequential z axis images were collected in 0.5-mm steps every 2 min. In these conditions, cells could enter mitosis and exit metaphase without any delay compared with cells recorded in phase–contrast only. Centriole tracking was performed automatically by Metamorph in maximal intensity projections computed from the original three-dimensional datasets.

Since Y-27632 is sensitive to light, cells were treated during 1 h with the drug before time-lapse recording, and the drug-containing medium was renewed at 1 h.

We thank Drs. C. Bosc and E. Denarier for continuous support and advice during this work.

This work was supported in part by a grant from Association por la Recherche sur le Cancer to D. Job.

Submitted: 7 March 2002
Revised: 15 April 2002
Accepted: 16 April 2002

References

Amano, M., Y. Fukata, and K. Kaibuchi. 2000. Regulation and functions of Rho-associated kinase. *Exp. Cell Res.* 261:44–51.

Andersen, S.S.L. 1999. Molecular characteristics of the centrosome. *Int. Rev. Cytol.* 187:51–109.

Bornens, M., M. Paintrand, J. Berges, M.C. Marty, and E. Karsenti. 1987. Structural and chemical characterization of isolated centrosomes. *Cell Motil. Cytoskeleton.* 8:238–249.

Chang, P., and T. Stearns. 2000. δ-Tubulin and ε-tubulin: two new human centrosomal tubulins reveal new aspects of centrosome structure and function. *Nat. Cell Biol.* 2:30–35.

Chevrier, V., S. Komesli, A.C. Schmit, M. Vantard, A.M. Lambert, and D. Job. 1992. A monoclonal antibody, raised against mammalian centrosomes and screened by recognition of plant microtubule organizing centers, identifies a pericentriolar component in different cell types. *J. Cell Sci.* 101:823–835.

Chevrier, V., M. Paintrand, V. Koteliansky, M.R. Block, and D. Job. 1995. Identification of vinculin as a pericentriolar component in mammalian cells. *Exp. Cell Res.* 219:399–406.

Euteneuer, U., and M. Schliwa. 1985. Evidence for an involvement of actin in the positioning and motility of centrosomes. *J. Cell Biol.* 101:96–103.

Frank, R. 1992. Spot-synthesis: an easy technique for the positionally addressable, parallel chemical synthesis on a membrane support. *Tetrahedron.* 48:9217–9232.

Fry, A.M., T. Mayor, P. Meraldi, Y.D. Stierhof, K. Tanaka, and E.A. Nigg. 1998a. C-Nap 1, a novel centrosomal coiled-coil protein and candidate substrate of the cell cycle-regulated protein kinase Nek2. *J. Cell Biol.* 141:1563–1574.

Fry, A.M., P. Meraldi, and E.A. Nigg. 1998b. A centrosomal function for the human Nek2 protein kinase, a member of the NIMA family of cell cycle regulators. *EMBO J.* 17:470–481.

Harborth, J., S.M. Elbashir, K. Bechert, T. Tuschl, and K. Weber. 2001. Identification of essential genes in cultured mammalian cells using small interfering RNAs. *J. Cell Sci.* 114:4557–4565.

Hinchcliffe, E.H., and G. Sluder. 2001. "It takes two to tango": understanding how centrosome duplication is regulated throughout the cell cycle. *Genes Dev.* 15:1167–1181.

Hirose, M., T. Ishizaki, N. Watanabe, M. Uehata, O. Kranenburg, W.H. Moolenaar, F. Matsumura, M. Maekawa, H. Bito, and S. Narumiya. 1998. Molecular dissection of the Rho-associated protein kinase (p160ROCK)–regulated neurite remodeling in neuroblastoma N1E-115 cells. *J. Cell Biol.* 141:1625–1636.

Holy, T.E., M. Dogterom, B. Yurke, and S. Leibler. 1997. Assembly and positioning of microtubule asters in microfabricated chambers. *Proc. Natl. Acad. Sci. USA.* 94:6228–6231.

Ishizaki, T., M. Maekawa, K. Fujisawa, K. Okawa, A. Iwamatsu, A. Fujita, N. Watanabe, Y. Saito, A. Kakizuka, N. Morii, and S. Narumiya. 1996. The small GTP-binding protein Rho binds to and activates a 160 kDa Ser/Thr protein kinase homologous to myotonic dystrophy kinase. *EMBO J.* 15:1885–1893.

Ishizaki, T., M. Naito, K. Fujisawa, M. Maekawa, N. Watanabe, Y. Saito, and S. Narumiya. 1997. p160ROCK, a Rho-associated coiled-coil forming protein kinase, works downstream of Rho and induces focal adhesions. *FEBS Lett.* 404:118–124.

Jean, C., Y. Tollon, B. Raynaud-Messina, and M. Wright. 1999. The mammalian interphase centrosome: two independent units maintained together by the dynamics of the microtubule cytoskeleton. *Eur. J. Cell Biol.* 78:549–560.

Kimura, K., T. Tsuji, Y. Takada, T. Miki, and S. Narumiya. 2000. Accumulation of GTP-bound RhoA during cytokinesis and a critical role of ECT2 in this accumulation. *J. Biol. Chem.* 275:17233–17236.

Komesli, S., F. Tournier, M. Paintrand, R. Margolis, D. Job, and M. Bornens. 1989. Mass isolation of calf thymus centrosomes: the identification of a specific configuration. *J. Cell Biol.* 109:2869–2878.

Kosako, H., T. Yoshida, F. Matsumura, T. Ishizaki, S. Narumiya, and M. Inagaki. 2000. Rho-kinase/ROCK is involved in cytokinesis through the phosphorylation of myosin light chain and not ezrin/radixin/moesin proteins at the cleavage furrow. *Oncogene.* 19:6059–6064.

Laemmli, U.K. 1970. Cleavage of structural proteins during the assembly of the head of bacteriophage T4. *Nature.* 227:680–685.

Lange, B.M.H., and K. Gull. 1995. A molecular marker for centriole maturation in the mammalian cell cycle. *J. Cell Biol.* 130:919–927.

Matsui, T., M. Amano, T. Yamamoto, K. Chihara, M. Nakafuku, M. Ito, T. Nakano, K. Okawa, A. Iwamatsu, and K. Kaibuchi. 1996. Rho-associated kinase, a novel serine/threonine kinase, as a putative target for the small GTP binding protein Rho. *EMBO J.* 15:2208–2216.

Mayor, T., Y.D. Stierhof, K. Tanaka, A.M. Fry, and E.A. Nigg. 2000. The centrosomal protein C-Nap1 is required for cell cycle-regulated centrosome cohesion. *J. Cell Biol.* 151:837–846.

Meraldi, P., and E.A. Nigg. 2001. Centrosome cohesion is regulated by a balance of kinase and phosphatase activities. *J. Cell Sci.* 114:3749–3757.

Mogensen, M.M., A. Malik, M. Piel, V. Bouckson-Castaing, and M. Bornens. 2000. Microtubule minus-end anchorage at centrosomal and non-centrosomal sites: the role of ninein. *J. Cell Sci.* 113:3013–3023.

Nakagawa, Y., Y. Yamane, T. Okanoue, S. Tsukita, and S. Tsukita. 2001. Outer dense fiber 2 is a widespread centrosome scaffold component preferentially associated with mother centrioles: its identification from isolated centrosomes. *Mol. Biol. Cell.* 12:1687–1697.

Narumiya, S., T. Ishizaki, and N. Watanabe. 1997. Rho effectors and reorganization of actin cytoskeleton. *FEBS Lett.* 410:68–72.

Narumiya, S., T. Ishizaki, and M. Uehata. 2000. Use and properties of ROCK-specific inhibitor Y-27632. *Meths. Enzymology.* 325:273–284.

Piel, M., P. Meyer, A. Khodjakov, C.L. Rieder, and M. Bornens. 2000. The respective contributions of the mother and daughter centrioles to centrosome activity and behavior in vertebrate cells. *J. Cell Biol.* 149:317–329.

Piel, M., J. Nordberg, U. Euteneuer, and M. Bornens. 2001. Centrosome-dependent exit of cytokinesis in animal cells. *Science.* 291:1550–1553.

Schliwa, M., U. Euteneuer, R. Graf, and M. Ueda. 1999. Centrosomes, microtubules and cell migration. *Biochem. Soc. Symp.* 65:223–231.

Tassin, A.M., and M. Bornens. 1999. Centrosome structure and Mt nucleation in animal cells. *Biol. Cell.* 91:343–354.

Tominaga, T., T. Ishizaki, S. Narumiya, and D.L. Barber. 1998. p160ROCK mediates RhoA activation of Na-H exchange. *EMBO J.* 17:4712–4722.

Towbin, H., T. Staehelim, and J. Gordon. 1979. Electrophoretic transfer of proteins from polyacrylamide gels to nitrocellulose sheets: procedure and some applications. *Proc. Natl. Acad. Sci. USA.* 76:4350–4354.

Ueda, M., R. Gräf, H.K. MacWilliams, M. Schliwa, and U. Euteneuer. 1997. Centrosome positioning and directionality of cell movements. *Proc. Natl. Acad. Sci. USA.* 94:9674–9678.

Uehata, M., T. Ishizaki, H. Satoh, T. Ono, T. Kawahara, T. Morishita, H. Tamakawa, K. Yamagami, J. Inui, M. Maekawa, and S. Narumiya. 1997. Calcium sensitization of smooth muscle mediated by a Rho-associated protein kinase in hypertension. *Nature.* 389:990–994.

Cell biology

Spinning actin to divide

Shuh Narumiya and Issei Mabuchi

When our cells divide, they are cut down the middle by a tightening belt of proteins. New work reveals that the protein filaments in this belt are made from scratch every time.

The ability of cells to multiply lies at the heart of many biological processes. In multicellular organisms such as ourselves, cell proliferation is essential for growth and development, and to replace cells spent by daily wear and tear. For single-celled species such as yeasts, proliferation is crucial because it is how these organisms reproduce. In order to proliferate, a cell has to duplicate its contents and then divide physically into two, distributing the duplicated contents evenly between the two new cells. This process of cell division — called cytokinesis — is carried out rather as if a thread encircling a boiled egg was gradually pulled tighter to constrict the egg and cut it across the middle. On page 82 of this issue, Pelham and Chang[1] provide a clear picture of how the cell spins such a thread.

The thread encircling a dividing cell is a belt of proteins called the contractile ring (Fig. 1) and — unlike the thread around the boiled egg — is constructed within the cell, just beneath the cell membrane. The ring is composed of actin filaments and myosin proteins, well-known components of muscle. It is thought to constrict when oppositely orientated actin filaments slide over each other with the help of myosin, just as in contracting muscle.

Actin filaments are long helical polymers of globular actin monomers. The conventional view of how the contractile ring forms is that ready-made actin filaments in the cell periphery are recruited to the site of cytokinesis during or after segregation of the genetic material (mitosis), and are assembled into the ring by myosin or by actin-bundling proteins. But last year it was shown in dividing frog eggs that actin monomers are rapidly incorporated into actin filaments in the contractile ring as it is being constructed, implying that formation of new actin filaments is required[2]. So what does happen? Pelham and Chang's detailed analysis[1] finds that the actin filaments are made from scratch and continuously assemble and disassemble. The authors also identify proteins that control this process.

All actin filaments form in two steps (Fig. 1). In the first — nucleation — three or four actin monomers assemble into a cluster, which acts as a seed. In the second step, called polymerization or elongation, monomers are successively added to the seeds, allowing rapid growth of the filament. Nucleation is the rate-limiting step, but is speeded up by a multiprotein complex named the Arp2/3 complex[3].

Pelham and Chang started by analysing the involvement of *de novo* actin-filament formation in the construction of the contractile ring in the fission yeast *Schizosaccharomyces pombe*, which divides in a similar way to mammalian cells. They used an *in vitro* test of ring assembly, which involves permeabilizing the dividing yeast cells, and incubating them with fluorescently labelled actin monomers. If actin nucleation and polymerization occur, the fluorescent monomers will be incorporated into the ring. Indeed, the authors found that a fluorescent ring was produced in these cells, and that ring formation was sensitive to an inhibitor of actin polymerization. In contrast, a drug that caps the rapidly growing ends of existing actin filaments did not affect the rate of actin incorporation into the ring. So the results imply that actin filaments are formed from scratch and *in situ* in the contractile ring.

Pelham and Chang then looked at the contribution of the Arp2/3 complex to actin dynamics in the permeabilized-cell system. They found, first, that mutant cells lacking Arp3 did not show actin incorporation. Second, antibodies that bind to Arp3 interfere with incorporation of actin into the contractile ring. So the Arp2/3 complex is necessary for formation of contractile-ring actin filaments, presumably at the nucleation step.

The authors also reveal that another means of controlling filament formation is involved in ring construction *in vivo* in *S. pombe*. This regulatory mechanism consists of two proteins, Cdc12 and Cdc3. Cdc12 is a member of the formin family of proteins, which are found in organisms from yeasts to mammals and include Bnl1 in budding yeast, Diaphanous in fruitflies and mDia in mammals[4]. Cdc3 is an actin-monomer-binding protein, also known as profilin. Formins related to Diaphanous bind profilin, and both are essential in cytokinesis[4,5].

Interestingly, the Arp2/3 complex and the formins have been shown to induce the formation of distinct actin structures: patches and cables, respectively, in budding yeast[6,7]; and lamellipodia (sheet-like cellular

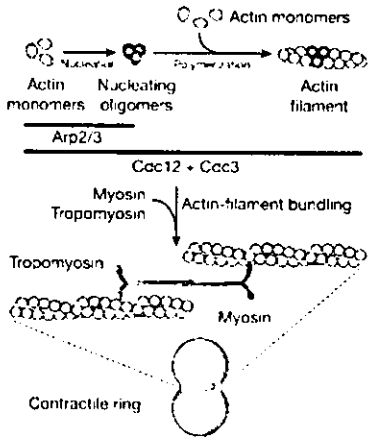

Figure 1 Spinning out the contractile ring. This ring, shown at the bottom, constricts to divide a proliferating cell into two. It is composed of antiparallel actin filaments, cross-linked by myosin molecules. Pelham and Chang[1] have found that the filaments are formed from scratch at the site of division, and continuously assemble and disassemble. The process of filament formation is shown from the top. First, actin monomers assemble into trimers ('nucleation'); trimers act as a seed to which further monomers are added ('polymerization'). Pelham and Chang find that the Arp2/3 complex and the Cdc12 and Cdc3 proteins are needed for nucleation or polymerization. The filaments are then organized into the contractile ring.

extensions) and stress fibres, respectively, in mammalian cells[3,8]. More intriguingly, the formin Bni1 can nucleate actin polymerization independently of the Arp2/3 complex *in vitro*, and the presence of profilin markedly accelerates subsequent polymerization[9,10]. It seems, then, that two mechanisms for actin nucleation and polymerization — one involving the Arp2/3 complex, and the other requiring formins and profilins — are recruited to, and work at, the site of cell division.

Finally, Pelham and Chang studied the stability of the contractile ring, and found that it is highly dynamic, with its components exchanging every minute. To show this, they used the technique of 'fluorescence recovery after photobleaching'. They tagged the protein tropomyosin or a subunit of myosin — both of which are actin-binding components of the contractile ring — with green fluorescent protein. When they bleached the fluorescence with laser light, they found that it recovered with a half-time of less than 30 seconds, indicating that the ring is broken down and reconstructed with new fluorescent components within this time period. Similar dynamics of myosin in the contractile ring have been reported previously[11], but the rate of exchange determined by Pelham and Chang is much faster. This requirement for a continuous supply of filament-binding proteins implies that not only actin polymerization, but also actin depolymerization, occurs in the ring, and explains the previously puzzling requirement for the actin-depolymerizing factor ADF/cofilin[12].

So Pelham and Chang[1] have shown that the contractile ring undergoes continuous remodelling to carry out its functions. Given the previous observations of dividing frog eggs[2], it seems that this mechanism is not limited to fission yeast, but applies more generally. What are the implications of these results? One of the authors' main findings is the need for the formin Cdc12 in ring construction. Although not explicitly shown for Cdc12, Diaphanous-related formins are targets of the Rho protein[4,5], which works as a molecular switch in various cell processes and has been suggested to regulate cytokinesis[13]. So this new study once again highlights the role of Rho in cell division. Studies of the functions and dynamics of Rho in cytokinesis might resolve several issues, such as how the plane of division is determined, and how the timing of cleavage is regulated.

Shuh Narumiya is in the Department of Pharmacology, Kyoto University Faculty of Medicine, Yoshida, Sakyo-ku, Kyoto 606-8501, Japan.
e-mail: snaru@mfour.med.kyoto-u.ac.jp
Issei Mabuchi is in the Department of Biology, School of Arts and Sciences, University of Tokyo, Komaba, Meguro-ku, Tokyo 153-8902, Japan.
e-mail: mabuchi@lins.u-tokyo.ac.jp

1. Pelham, R. J. & Chang, F. *Nature* **419**, 82–86 (2002).
2. Noguchi, T. & Mabuchi, I. *J. Cell Sci.* **114**, 401–412 (2001).
3. Higgs, H. N. & Pollard, T. D. *Annu. Rev. Biochem.* **70**, 649–676 (2001).
4. Wasserman, S. *Trends Cell Biol.* **8**, 111–115 (1998).
5. Watanabe, N. *et al. EMBO J.* **16**, 3044–3056 (1997).
6. Evangelista, M. *et al. Nature Cell Biol.* **4**, 32–41 (2002).
7. Sagot, I., Klee, S. K. & Pellman, D. *Nature Cell Biol.* **4**, 42–50 (2002).
8. Watanabe, N. *et al. Nature Cell Biol.* **1**, 136–143 (1999).
9. Pruyne, D. *et al. Science* **297**, 612–615 (2002).
10. Sagot, I. *et al. Nature Cell Biol.* **4**, 626–631 (2002); advance online publication, 22 July 2002 (doi:10.1038/ncb834).
11. Wong, K. C. Y. *et al. Curr. Biol.* **12**, 724–729 (2002).
12. Abe, H. *et al. J. Cell Biol.* **132**, 871–885 (1996).
13. Mabuchi, I. *et al. Zygote* **1**, 325–331 (1993).

Multiple spatiotemporal modes of actin reorganization by NMDA receptors and voltage-gated Ca^{2+} channels

Tomoyuki Furuyashiki*, Yoshiki Arakawa*, Sayaka Takemoto-Kimura*, Haruhiko Bito*†‡, and Shuh Narumiya*

*Department of Pharmacology, Kyoto University Faculty of Medicine, and †Precursory Research for Embryonic Science and Technology, Japan Science and Technology Corporation, Sakyo-ku, Kyoto 606-8315, Japan

Edited by Richard W. Tsien, Stanford University School of Medicine, Stanford, CA, and approved August 22, 2002 (received for review March 14, 2002)

Cytoskeleton is believed to contribute to activity-dependent processes underlying neuronal plasticity, such as regulations of cellular morphology and localization of signaling proteins. However, how neuronal activity controls actin cytoskeleton remains obscure. Taking advantage of confocal imaging of enhanced GFP-actin in the primary culture of hippocampal neurons, we show that synaptic activity induces multiple types of actin reorganization, both at the spines and at the somatic periphery. Activation of *N*-methyl-D-aspartate receptors, accompanied with a local rise in $[Ca^{2+}]i$, was sufficient to trigger a slow and sustained recruitment of actin into dendritic spines. In contrast, opening of voltage-gated Ca^{2+} channels rapidly and reversibly enhanced cortical actin at the somatic periphery but not in the spines, in keeping with a high transient rise in somatic $[Ca^{2+}]i$. These data suggest that spatiotemporal dynamics of $[Ca^{2+}]i$, triggered by activation of *N*-methyl-D-aspartate receptors and voltage-gated Ca^{2+} channels, provides the molecular basis for activity-dependent actin remodeling.

Establishment and remodeling of neural connections require a spatially and temporally orchestrated control of neuronal morphology (1, 2) and fine-tuning of assemblies of signaling complexes (3–8). Although such dynamic reorganization is common during embryonic development, recent evidence indicated that, even in mature brain tissues, neuronal activity may initiate and regulate the active modification of cell shape (9–15) and the sorting of neuronal molecules (16–19). *In vitro* studies suggest the requirement for an actin-based mechanism in dendritic spine motility (20, 21) as well as in localization of synaptic proteins at the postsynaptic density (22). These lines of evidence indicate the importance of cytoskeletal signaling in regulating neuronal properties even after their functional maturation.

Despite a growing interest in the role of actin remodeling during activity-dependent modification of neuronal properties, the fundamental question as to how neuronal activity regulates actin filaments has not been settled. For instance, neuronal activity has been associated with either an increase (9, 11, 14, 15) or a decrease (10, 13) in the number of dendritic spines. Furthermore, intracellular Ca^{2+} rise seemed to give rise to opposite effects on actin cytoskeleton. Ca^{2+}-dependent accumulation of actin has been reported in goldfish retinal bipolar cells (23) and in developing grasshopper neurons (24), whereas others have found an *N*-methyl-D-aspartate (NMDA)-stimulated actin dislocation at dendritic spines (25, 26). These apparently conflicting observations raise the possibility that activity-dependent regulation of actin reorganization may be ruled by multiple coexisting modes of signaling from synapse to cytoskeleton.

Setting aside such controversy, most studies have similarly argued that intracellular Ca^{2+} is involved in actin reorganization (23–27). Recent pharmacological evidence has highlighted the diversity of Ca^{2+} entry sources, each of which may have distinct functions in various cellular phenomena, such as synaptic plasticity (for review, see ref. 4) and gene expression (28). Previous work on Ca^{2+}-induced actin responses indeed used various kinds of stimulation protocols which were likely to activate distinct routes of Ca^{2+} entry. Thus, the reported dichotomy in Ca^{2+}-mediated actin responses might reflect the functional segregation of different Ca^{2+} sources, each contributing distinctly during actin reorganization. To gain definitive insights into these issues, we visualized directly actin dynamics in live, synaptically connected, cultured hippocampal neurons by use of enhanced GFP (EGFP)-actin and analyzed Ca^{2+}-based mechanisms in activity-dependent actin reorganization.

Materials and Methods

Construction of the adenovirus which expresses EGFP-actin, the primary culture of hippocampal neurons, adenoviral infection, pharmacological and electrical stimulations, imaging of EGFP-actin and vital fluorescent dyes (FM4–64, Fluo-4/AM, and Fura-2/AM), digital processing of these fluorescent images, and statistical data analyses were performed as described with minor modifications. The detailed information about these experimental procedures is provided in *Additional Text About Materials and Methods*, which is published as supporting information on the PNAS web site, www.pnas.org. All images were acquired at room temperature in Tyrode solution supplemented with appropriate drugs. All fluorescence values of EGFP-actin had been normalized to their prestimulus values before they were subjected to the quantitative analyses. The distinction between different actin structures (the punctate and the cortical accumulations) was determined according to their shapes and sizes (see *Additional Text* in supporting information). In the ratiometric Ca^{2+} imaging experiments, we included 5 μM ω-conotoxin MVIIC during all stimulations to remove the contamination of presynaptic Ca^{2+} transients triggered by opening of N- or P/Q-type Ca^{2+} channels and because bath application of Cd^{2+} significantly quenched Fura-2 fluorescence. This manipulation by itself did not affect actin dynamics induced by high K^+.

Results

Synaptic Activity Induced Multiple Types of Actin Reorganization at Distinct Subcellular Sites. To introduce EGFP-actin to synaptically connected cultured hippocampal neurons with minimal toxicity, we constructed an adenovirus which expresses EGFP-actin (for the detailed characterization of EGFP-actin properties, see Fig. 6, which is published as supporting information on the PNAS web site). EGFP-actin was localized to dendritic spines (see Fig. 7, which is published as supporting information on the PNAS web site), in close agreement with reports of endogenous actin molecules (29, 30). Furthermore, synapses and dendritic spines were formed intact in the presence of EGFP-actin (data not

This paper was submitted directly (Track II) to the PNAS office.

Abbreviations: EGFP, enhanced GFP; VGCCs, voltage-gated Ca^{2+} channels; NMDA, *N*-methyl-D-aspartate; ROI, region of interest.

‡To whom correspondence should be addressed. E-mail: hbito@mfour.med.kyoto-u.ac.jp.

www.pnas.org/cgi/doi/10.1073/pnas.212148999

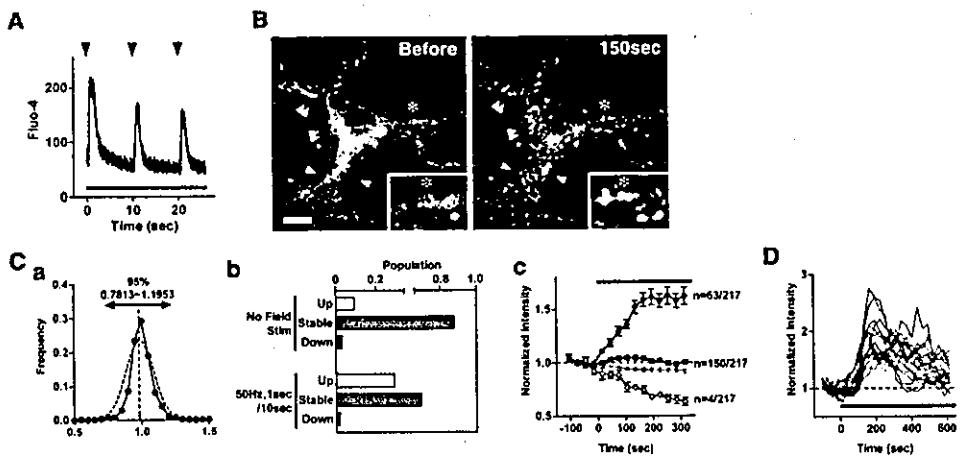

Fig. 1. Electrically patterned synaptic activity induces enhancement of actin puncta in spine-like structures. (*A*) The fluorescence intensity of Fluo-4 in a neuronal cell body was measured in the line-scan mode. Trains at 9-s intervals (arrowheads) were continuously applied by using field stimulation electrodes throughout the duration of the recording (bar). (*B*) Significant numbers of punctate accumulation of EGFP-actin (arrowheads) were detected at the 150-s time point during the same stimulus train as in *A*. The magnified and smoothed image is shown in *Inset*. **, same position. (Bar = 10 μm.) See also Movie 1. (*Ca*) Distribution of basal EGFP-actin fluorescence (solid line) and its Gaussian-fitted curve (dotted line). EGFP-actin fluorescence intensity was normalized to average intensity. Ninety-five percent of puncta were included in the 0.7813–1.1953 interval (mean ± 2 SD). (*Cb*) Electrical field stimulation augments the number of puncta with a fluorescence increase greater to 2 SD ("Up", >1.1953-fold of the mean) while diminishing the number of puncta with a lesser increase ("Stable", changes smaller than 2 SD; "Down", decrease greater than 2 SD). Two hundred and seventeen puncta from 8 stimulated neurons and 65 puncta from 4 unstimulated neurons were analyzed. (*Cc*) Temporal profiles of averaged fluorescence intensity in the three categories ("Up", ●; "Stable", ■; "Down", ○). The total integrated fluorescence from all pixels in the soma area is also shown (red line). (*D*) Individual traces of EGFP-actin fluorescence from 18 puncta showing fluorescence increase (>SD) in a single representative neuron. The same stimulus as in *A* was applied (bar). Data are shown as means ± SEM.

shown). These data verified EGFP-actin as a suitable tracer of endogenous actin molecules.

Taking advantage of confocal time-lapse imaging of EGFP-actin expressed in cultured hippocampal neurons, we asked whether and how actin dynamics are controlled by synaptic activity. First, we applied continuous trains of electrical pulses to trigger synaptic activity by means of extracellular field stimulation. However, a train of electrical pulses delivered at even as high as 50 Hz was unable to induce a detectable change in actin localization (data not shown). Based on Ca^{2+} imaging, we suspected that the failure of EGFP-actin response might be caused by the lack of sustained increase in $[Ca^{2+}]i$ during prolonged application of continuous electrical trains. After optimization of stimulus patterns for the maximal Ca^{2+} increase, we found that bursts of 50-Hz, 1-s stimuli delivered continuously at 9-s intervals (Fig. 1*A*) elicited reliable changes in punctate EGFP-actin signals, most likely at dendritic spines, when given after 12-h pretreatment with tetrodotoxin (TTX) followed by its washout (15 of 23 neurons; Fig. 1*B*; 18 ± 3% increase from baseline at 315 s after the initiation of the stimulus in 8 neurons; $P < 0.0001$; see Fig. 8*A* and Movie 1, which are published as supporting information on the PNAS web site). In contrast, little change was detected in nonstimulated control neurons (3 ± 5% increase at the same time point above, $P > 0.5$). It should also be noted that the distribution of EGFP fluorescence was not altered throughout field stimulation in cultured hippocampal neurons expressing EGFP (5 neurons, Fig. 8*B*). Thus, the recorded events were unlikely to be artifacts caused by cell toxicity, photodamage, or local modification of EGFP fluorescence property.

To examine the spine-to-spine variability in the activity-induced actin response, we compared the temporal profile of the fluorescence changes for each EGFP-actin puncta following the stimulation above. The basal fluctuation of fluorescence values of individual puncta was well fitted with a single Gaussian (Fig. 1*Ca*); a two-fold standard deviation (SD) was used as a threshold to assess the statistical significance of stimulus-dependent changes. In the absence of stimuli, the fluorescence values changed little, with few puncta showing a change in fluorescence exceeding 2 SD (9.2%, Fig. 1*Cb*, upper half). In contrast, when a 50-Hz, 1-s burst field stimulation was applied every 10 s, about 30% of the puncta revealed a fluorescence increase exceeding 2 SD (29%; Fig. 1*Cb*, lower half and Fig. 1*Cc*). The change in fluorescence properties of EGFP itself was negligible as the total sum of fluorescence in the soma varied little (8 ± 2% decrease

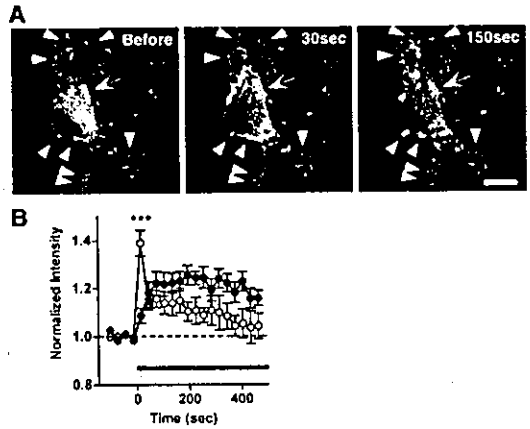

Fig. 2. Rapid induction and decay of cortical actin enhancement is also triggered by patterned synaptic activity. (*A*) A representative neuron showing both cortical (arrow) and punctate (arrowheads) accumulations of EGFP-actin. (Bar = 10 μm.) (*B*) Punctate (●, 16 ROIs from 2 neurons) and cortical (○, 9 ROIs from 2 neurons) actin accumulations revealed a striking difference in activation and decay kinetics during the whole duration of the field stimulation (shown by bar). All data are shown as means ± SEM. ***, $P < 0.001$.

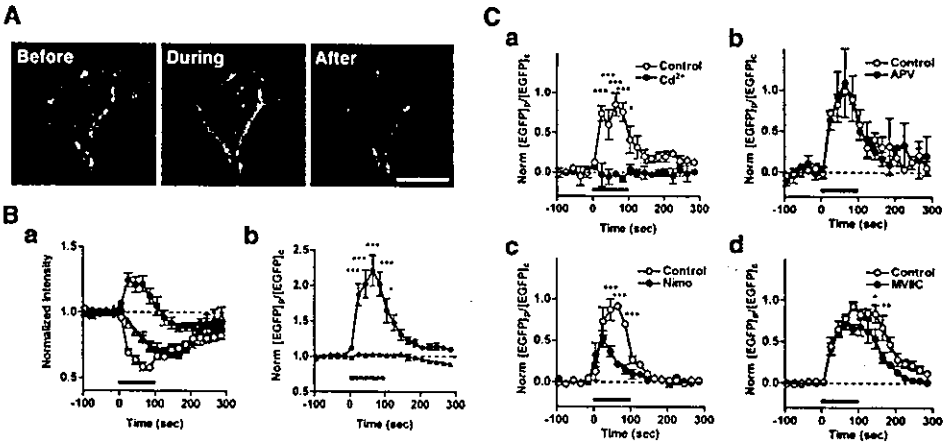

Fig. 3. High K^+-induced depolarization elicited rapid and reversible accumulation of EGFP-actin to the somatic periphery through the opening of voltage-gated Ca^{2+} channels. (*A*) EGFP-actin (green) distribution before, during, and after depolarization with 90 mM K^+ in a hippocampal neuron, with a simultaneous recording of the decay of FM4–64 signals (red). See also Movie 2. (Bar = 15 μm.) (*Ba*) Traces of EGFP-actin (13 neurons, ● and ○) or EGFP (4 neurons, ▲ and △) intensity at the somatic periphery (the single brightest ROI at the edge of the EGFP-actin signals at the soma, ● and ▲) and the bulk cytoplasm (the single darkest ROI at the perinuclear region, ○ and △). (*b*) The ratio of the fluorescence intensity at the somatic periphery and the bulk cytoplasm ([EGFP]p/[EGFP]c), normalized to the value before stimulation, as the translocation index for EGFP signals (●, EGFP-actin; ▲, EGFP). (*C a–d*) The dependence of high K^+-induced increases in [EGFP]p/[EGFP]c on various Ca^{2+} influx sources was examined in the absence (○) or presence (●) of various reagents such as 100 μM Cd^{2+} (*a*, 4 neurons), 50 μM D-APV (*b*, 3 neurons), 10 μM nimodipine (*c*, 3 neurons), or 5 μM ω-conotoxin MVIIC (*d*, 4 neurons). All data were rescaled based on the peak value during the control depolarization (○), applied 10 min before the second depolarization in the presence of the reagents (●). Repeated depolarization reliably induced the cortical actin accumulation (data not shown). Stimulus duration was shown by bar for each dataset. *, $P < 0.05$; **, $P < 0.01$; ***, $P < 0.001$. All of the plots are shown in means ± SEM.

at 315 s after the beginning of the stimulus; Fig. 1*Cc*, red line). Thus, synaptic stimulation induced a slow and sustained enhancement of EGFP-actin fluorescence in many, but not all, dendritic spines. Superimposed individual fluorescence profiles from one neuron, whose increase exceeded 1 SD, are shown in Fig. 1*D*. A relative synchrony in the rising time was observed across many spines within the same neuron during the initial accumulation phase. In contrast, a greater variability seemed to exist for the decay kinetics across different puncta. This seems to be caused, at least in part, by the fact that a small subgroup of puncta showed a sustained enhancement throughout the observation period, whereas most of the punctate accumulations gradually decayed to their original level.

In addition to the punctate accumulation, the brightness of EGFP-actin also significantly augmented at the somatic periphery (9 of 23 neurons, Fig. 2*A*). Interestingly, in six neurons, a rise in EGFP-actin signals also was found in dendritic spines in parallel with an increase in the cortical signals, allowing direct comparison of the kinetics between these two types of actin accumulation. Both the accumulation phase and the decay phase occurred significantly faster for the cortical actin than for the punctate enhancement (Fig. 2*B*). Such diversity in the temporal and spatial patterns of actin relocation is most consistent with the presence of multiple modes of activity-dependent actin reorganization within a single neuron.

Voltage-Gated Ca^{2+} Channels, but Not NMDA Receptors, Are Essential for Actin Accumulation to the Somatic Periphery. To determine what kind of synaptic activity directly triggers actin relocation, we examined the contribution of various Ca^{2+} entry sources. Massive depolarization was first applied by increasing the extracellular K^+ concentration from 5 mM to 90 mM (high K^+). As shown in Fig. 3 *A* and *B* (see also Movie 2, which is published as supporting information on the PNAS web site), this stimulus induced a rapid decrease in the diffuse cytoplasmic EGFP-actin signal in the soma, whereas a robust concentration of EGFP-actin was observed at the cell periphery. The latter change was reminiscent of the cortical accumulation induced by field stimulation. Such complementary changes in cytoplasmic and peripheral EGFP-actin signals indicate that actin massively relocated from the bulk cytoplasm to the cell periphery. These changes persisted throughout the duration of the depolarization, and were reversed upon its cessation (Fig. 3 *A* and *B*). By using [EGFP]p/[EGFP]c (see the legend of Fig. 3*Bb*) as an index for high K^+-induced actin relocation, the half-rising time of activation was found to be less than 30 s, whereas the half-decay time constant was on the order of 1 min (Fig. 3*Bb*). Acquisition of vertically sliced images revealed that high K^+ induced a linear enhancement of EGFP-actin signals at the lateral side but not at the top or at the bottom of the soma (Fig. 9, which is published as supporting information on the PNAS web site). In EGFP-expressing neurons, the same stimulus caused a uniform rate of decrease in the fluorescence signals at the somatic periphery and the cytoplasm (Fig. 3*Ba*), thus keeping the ratio of [EGFP]p/[EGFP]c constant (Fig. 3*Bb*).

Because removal of extracellular Ca^{2+} eliminated high K^+-induced actin relocation as determined under live or fixed conditions (data not shown), we next tested the specific contribution of several Ca^{2+} entry sources. Blockade of high voltage-activated (HVA) Ca^{2+} channels using Cd^{2+} (100 μM) abolished the cortical accumulation of EGFP-actin signals (Fig. 3*Ca*: 104% reduction from the control at 25 s after initiation of the stimulus, $P < 0.001$). In contrast, inhibition of NMDA receptors using D-APV (50 μM) had no significant effect (Fig. 3*Cb*: 12% reduction from the control at 25 s after initiation of the stimulus, $P > 0.05$). These data implied that Ca^{2+} entry through VGCCs may be critical for actin relocation induced by high K^+, whereas they failed to support a role of NMDA receptors in these processes. In keeping with this idea, nimodipine, a selective blocker for L-type VGCC, significantly blocked the maintenance phase of actin relocation (Fig. 3*Cc*; 78% reduction from the control at 85 s, $P < 0.001$), but not its initiation phase (Fig. 3*Cc*: 30% reduction from the control at 25 s, $P > 0.05$). In contrast, ω-conotoxin MVIIC at a dose known to inhibit N- and P/Q-type Ca^{2+} channels had a marginal effect on either phase (Fig. 3*Cd*:

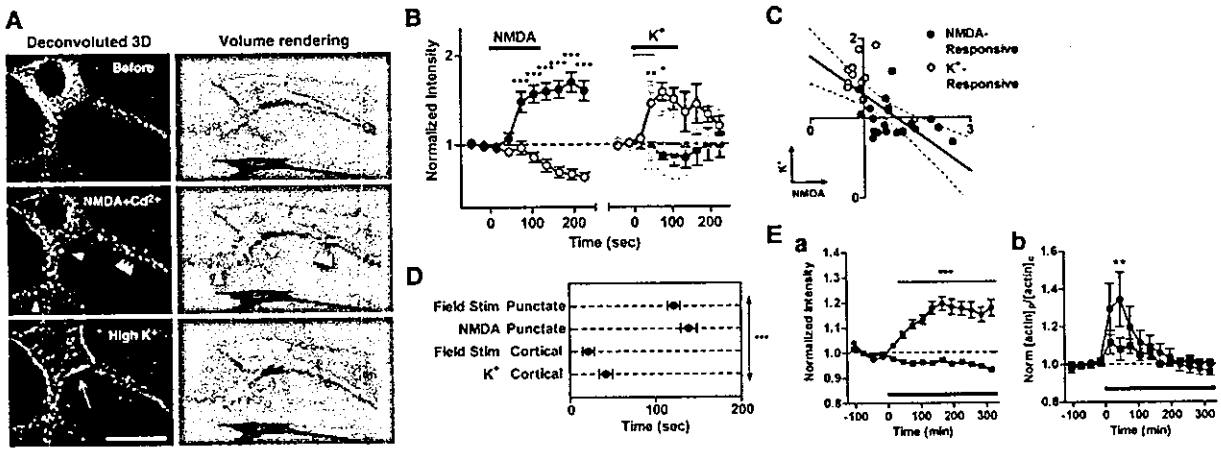

Fig. 4. Activation of NMDA receptors induced actin accumulation to the dendritic spines, but not to the somatic periphery. (*A Left*) Deconvoluted 3-D images of typical EGFP-actin distribution within the same hippocampal neuron, before (Before), after NMDA application with Cd^{2+} (NMDA+Cd^{2+}), and after a subsequent high K^+ depolarization following washout of NMDA and Cd^{2+} (High K^+). See also Movie 3. (Bar = 20 μm.) (*A Right*) A 3-D-rendered pseudocolor illustration of the distribution of NMDA-induced and high K^+-induced EGFP-actin accumulations in the panels at *Left*. EGFP-actin-enriched structures are illustrated in yellow; they are based on the arbitrary threshold (arrowheads and an arrow). The signals of EGFP-actin below the threshold are shown in red. (*B*) Temporal profiles of averaged EGFP-actin fluorescence at typical NMDA-responsive (●, 22 ROIs from 3 neurons) or high K^+-responsive (○, 10 ROIs from 3 neurons) regions. An increase exceeding 2 SD was considered as a significant response. High K^+ did not alter the fluorescence intensity at EGFP-actin puncta, irrespective of the stimulus duration (2 min, black, 1 neuron; 1 min, gray, 2 neurons). (*C*) Correlative plots of each individual ROI in *B*. Increases in EGFP-actin fluorescence during stimulation with NMDA (at 105 s) and with high K^+ (at 45 s) at either the NMDA-responsive or the high K^+-responsive regions are compared. Note that there are two distinct clusters with different responsiveness toward each stimulus. The responsiveness to NMDA and to high K^+ shows a negative correlation (slope of linear regression = -0.4855 ± 0.1181, $P < 0.001$, F test). The dotted line shows a 95% confidence interval for linear regression. (*D*) Averaged 0–80% rising times ($\tau_{0.8}$) are calculated and compared for the cortical and punctate actin accumulations induced by field stimulation and for NMDA- and high K^+-stimulation. (*E*) The punctate actin accumulation (*a*) was abolished in the presence of D-APV (50 μM or 100 μM, ■, 150 puncta from 10 neurons; ●, control trace). The cortical accumulation (*b*), which is quantified in the translocation index of [EGFP]p/[EGFP]c as in Fig. 3, was still induced by field stimulation in the presence of D-APV, although to a significantly lesser degree [11 neurons each with (■) or without (●) D-APV]. Data is shown as means ± SEM. *, $P < 0.05$; **, $P < 0.01$; ***, $P < 0.001$. Bars indicate stimulus duration.

7 and 30% decrease at 25 and 85 s, respectively, $P > 0.05$). These results are consistent with the involvement of multiple types of HVA Ca^{2+} channels in high K^+-induced cortical actin accumulation.

Activation of NMDA Receptors Induces Local Changes in Actin at the Spines but Not at the Somatic Periphery. At the hippocampal CA1 excitatory synapses, glutamatergic synaptic inputs induce significant amount of Ca^{2+} influx via NMDA receptors (31–33). It also has been shown that local electrical stimulation induces NMDA receptor-dependent changes in dendritic morphology (11, 14). We asked whether actin redistribution could be elicited by activation of NMDA receptors themselves, and thus stimulated the neurons with 100 μM NMDA in Mg^{2+}-free solution containing Cd^{2+} (100 μM; NMDA+Cd^{2+}). After preincubation with TTX, stimulation of NMDA receptors for a few minutes induced a prominent increase in the EGFP-actin fluorescence intensity in a significant proportion of synaptic puncta (Fig. 4*A*, arrowheads; see also Fig. 10 and Movie 3, which are published as supporting information on the PNAS web site) juxtaposed to FM4–64-positive spots (Fig. 11, which is published as supporting information on the PNAS web site). This result seems to be in contrast to the previous studies suggesting NMDA-induced actin depolymerization at dendritic spines (25, 26). However, it should be noted that, unlike in these previous articles, we completely blocked HVA Ca^{2+} channels to achieve pure NMDA stimulation. Although a number of puncta also showed an activity-dependent decrease in fluorescence (Fig. 10*B*), the decrease was comparable to the general loss of fluorescence from the cell soma (red line in Fig. 10*B*; $P > 0.05$ at any time point).

We next sequentially stimulated the same neurons with NMDA+Cd^{2+} and then with high K^+. As described above, initial stimulation with NMDA+Cd^{2+} induced a punctate accumulation of EGFP-actin signals in the spines (Fig. 4 *A* and *B*). After removal of NMDA and a 10-min washout, the punctate accumulation disappeared (Fig. 11). Even after the washout of Cd^{2+}, application of high K^+ failed to elicit the punctate accumulation previously induced by NMDA (Fig. 4 *A* and *B*). Instead, robust appearance of the cortical EGFP-actin accumulation was observed (Fig. 4*A*, arrow). The correlative plot of the fluorescence increase at individual spots upon NMDA and high K^+ stimuli further confirmed the specificity of the type of stimuli that potently trigger actin accumulation on a given local area (Fig. 4*C*). A similar result was obtained when the order of the stimuli was reversed (data not shown, 2 neurons) or when actin relocation was determined by immunostaining on fixed samples (Fig. 12, which is published as supporting information on the PNAS web site).

To compare the appearance of several types of activity-induced actin enhancement, we carried out quantitative analyses of accumulation kinetics after each kind of stimuli. NMDA+Cd^{2+} induced punctate accumulation with a time constant of 0–80% rise ($\tau_{0.8}$) of about 2 min (139 ± 9 s), whereas $\tau_{0.8}$ for high K^+ was about 40 s (42 ± 8 s, Fig. 4*D*). These time constants were comparable to $\tau_{0.8}$ of the punctate actin accumulation (122 ± 7 s) and that of the cortical actin accumulation (22 ± 7 s) during field stimulation, respectively. These data indicated the specific requirement of distinct Ca^{2+} sources for each type of synaptically induced actin structures. Indeed, D-APV strongly inhibited the punctate actin accumulation induced by field stimulation, whereas the cortical accumulation could still be induced in the presence of D-APV, although to a significantly lower degree (Fig. 4*E*). Therefore, Ca^{2+} entry via HVA Ca^{2+} channels and NMDA receptors is likely to cause distinct and complementary patterns of actin relocation upon synaptic stimulation.

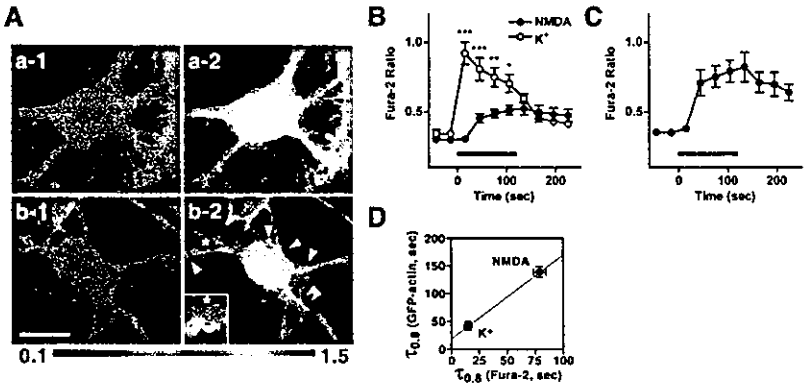

Fig. 5. Spatial and temporal Ca^{2+} dynamics is tightly linked with activity-dependent actin reorganization following high K^+ and NMDA-stimuli. (*A*) Ratiometric measurements of Fura-2 fluorescence excited at 340 nm and at 380 nm before (*a-1, b-1*) and at 105 s during stimuli (*a-2, b-2*) in neurons stimulated with high K^+ (*a*), and in those stimulated with NMDA in the absence of Mg^{2+} and in the presence of nimodipine (*b*). All Ca^{2+} imaging was performed in the presence of 5 μM ω-conotoxin MVIIC to avoid the contamination of large Ca^{2+} increase at presynaptic terminals. Localized Ca^{2+} transients (*b-2*, white arrowheads) were observed only in NMDA-stimulated cells. Stimulus duration was 2 min for each stimulus. A magnified and smoothed view of a typical local dendritic Ca^{2+} rise is shown in *Inset*. The asterisk in each image shows the same position. (*B*) Comparison of Ca^{2+} transients at the somatic periphery upon high K^+ (○, 4 neurons) or NMDA (●, 11 neurons) stimulation. Note the distinction in the amplitude and the kinetics of the two responses. (*C*) Slow but robust Ca^{2+} transients are induced at localized puncta in the dendrites and the soma upon NMDA activation—36 ROIs from 11 neurons. (*D*) Correlation between $\tau_{0.8}$ for induced Ca^{2+} transients and actin responses. Data are shown as means ± SEM. *, $P < 0.05$; **, $P < 0.01$; ***, $P < 0.001$. Bars indicate stimulus durations.

A Link Between Spatiotemporal Modulation of $[Ca^{2+}]i$ by NMDA Receptors and Voltage-Gated Ca^{2+} Channels and Activity-Dependent Actin Recruitment. Local control of Ca^{2+} dynamics provides a mechanism for tight regulation of actin behavior and actin-based contractility in smooth muscles (34), but this has not been tested fully in neurons. Thus, we tried to analyze whether distinct actin responsiveness toward NMDA receptors and VGCCs may be controlled directly by Ca^{2+} dynamics through these channels. Ratiometric Ca^{2+} imaging using Fura-2/AM-loaded neurons indicated that high K^+-stimulated hippocampal neurons underwent a massive and global, but reversible, rise in $[Ca^{2+}]i$ throughout the cell (Fig. 5 *Aa* and *B*). In contrast, NMDA application in the absence of Mg^{2+} and in the presence of nimodipine only resulted in a slower and smaller $[Ca^{2+}]i$ increase in most parts of the neurons, which persisted even after the cessation of the stimuli (Fig. 5 *Ab* and *B*). However, a large and sustained increase in $[Ca^{2+}]i$ was recorded as localized puncta on the dendrites and the soma (Fig. 5 *Ab-2* and *C*). The amplitude of this localized Ca^{2+} response ("Ca^{2+} hotspots") was comparable to that induced by high K^+ at the somatic periphery. These Ca^{2+} hotspots were induced in an NMDA-specific and stimulus-dependent manner (Fig. 5*A* and Fig. 13, which is published as supporting information on the PNAS web site).

To gain insight into the relationship between Ca^{2+} increase and EGFP-actin accumulation, $\tau_{0.8}$ for rise in $[Ca^{2+}]i$ and EGFP-actin fluorescence were compared. The global and rapid rise in $[Ca^{2+}]i$ induced by high K^+ occurred with $\tau_{0.8}$ of about 15 s (15 ± 0 s), coincident with the rapid initiation of the high K^+-induced cortical recruitment of actin ($\tau_{0.8}$ = 42 ± 8 s, Fig. 5*D*). In contrast, NMDA-induced rise in $[Ca^{2+}]i$ appeared with a significantly larger time constant ($\tau_{0.8}$ = 79 ± 6 s, $P < 0.0001$ compared with $\tau_{0.8}$ for high K-induced $[Ca^{2+}]i$ rise, Fig. 5*D*). The NMDA-induced EGFP-actin recruitment was initiated at the similar time constant as $[Ca^{2+}]i$ (Fig. 5*D*, $\tau_{0.8}$ = 139 ± 9 s). Therefore, an apparent correlation was observed between $\tau_{0.8}$ for $[Ca^{2+}]i$ mobilization and actin reorganization induced by either high K^+ or NMDA stimulus. Taken together, our data suggest that distinction in Ca^{2+} dynamics based on Ca^{2+} entry sources plays a dominant role in directing spatiotemporal patterns of activity-induced actin reorganization (Fig. 14, which is published as supporting information on the PNAS web site).

Discussion

Actin filaments are major components of the cytoskeleton at the postsynaptic sites of the excitatory synapses (29, 30). The bivalent nature of actin cytoskeleton dynamics, rigidity, and plasticity has attracted neurobiologists for decades as a possible molecular basis that may account for certain kinds of synaptic plasticity (30). In this study, we report three main observations concerning activity-induced actin responses in hippocampal neurons.

First, certain patterns of synaptic activity, triggered through extracellular field stimulation, induce actin accumulation at dendritic spines and at the somatic periphery as rapidly as in the order of minutes. It is noteworthy that maximal actin accumulation to dendritic spines could only be observed after prior silencing of endogenous neuronal activity (see the discussion in *Additional Text*), adding to the notion that activity-dependent actin regulation is highly dependent on the context in which a neuron receives synaptic inputs.

Second, spatiotemporal dynamics in $[Ca^{2+}]i$ triggered by either VGCCs or NMDA receptors is coupled with two separate types of activity-induced actin accumulations with regard to their onset kinetics (fast vs. slow), subcellular distribution (somatic periphery vs. dendritic spines), and duration (transient vs. persistent). The high correlation between the onset kinetics of actin accumulations and $[Ca^{2+}]i$ upon NMDA and high K^+ stimulation is consistent with the possibility that a uniform biochemical process is involved in the conversion of Ca^{2+} entry into actin recruitment. The fact that NMDA receptors are enriched at the synapse (for example, see ref. 19), whereas L-type VGCC is more diffusely distributed at the somatodendritic region (35) implies that the actin reorganizations in this study occurred at the subcellular loci physically close to Ca^{2+} entry sites. Thus, we favor the simplest view that Ca^{2+} influx through distinct types of Ca^{2+} entry channels locally activates actin regulatory mechanisms, resulting in a high correlation between the spatiotemporal properties of Ca^{2+} dynamics and actin reorganization. However, it should also be noticed that either punctate or cortical actin reorganization occurs at only a fraction of those regions expressing responsible Ca^{2+} entry channels. This result suggests that factors yet unrevealed may further contribute to the ultimate outcome of actin behaviors. Detailed analyses of actin regulatory mechanisms within each spine are necessary for elucidating fully

the molecular basis by which spatial distribution of actin reorganization is determined.

Third, we found that activity-induced actin accumulation is heterogeneous in nature across individual dendritic spines. This finding is supported by two observations. First, we observed that some, but not all, spines in a single neuron show an increase in actin content upon synaptic or NMDA-receptor activation (Fig. 1*C* and Fig. 10). Second, even across those spines where actin accumulation was recorded, there was considerable heterogeneity in the decay kinetics, such that the spine actin content was increased more persistently in some spines than in others (Fig. 1*D*). Therefore, it is likely that actin content could be separately controlled at the single-spine level. This view is consistent with a previous report suggesting that local elevation of intracellular Ca^{2+} leads to localized actin enhancement in grasshopper neurons (24). To clarify fully the independence of actin regulation at individual spines, local activation of excitatory synapses by use of local application of high K^+ or glutamate, with all neighboring synapses silenced, remains to be carried out.

In conclusion, we found that synaptic activity induces multiple modes of actin reorganization of discrete spatial and temporal patterns, each of which is driven by a distinct Ca^{2+} entry source. It highlights the notion that spatiotemporal control of actin reorganization is tightly coupled to complex patterns of synaptic inputs and underlying Ca^{2+} dynamics. Whether and how such specificity in Ca^{2+}-actin coupling could contribute to activity-dependent controls of spine morphology and protein localization underlying synaptic plasticity awaits future studies.

We thank Roger Y. Tsien (University of California at San Diego) and Atsushi Miyawaki (RIKEN-Brain Science Institute, Wako, Japan) for advice on GFP mutants; Hirohide Takebayashi (National Institute for Physiological Sciences, Okazaki, Japan) for technical advice on the adenovirus construction; Fumiyoshi Ishidate, Kazunori Sugai, and Shigeki Yokoyama (Carl Zeiss, Japan) for providing access to the HUYGENS SYSTEM V.2.1.7 (Scientific Volume Imaging, Hilversum, The Netherlands) and IMARIS V.2.7 (Bitplane, Zurich); Kimiko Nonomura for technical assistance; and Tae Arai and Hiroko Nose for secretarial help. This work was supported by Grants-in-Aid from the Ministry of Education, Culture, Sports, Science and Technology of Japan (to S.N. and H.B.) and the Ministry of Health of Japan (to H.B.), and Research Grants from the Asahi Glass Foundation, the Cell Science Research Foundation, the Nissan Science Foundation, the Tanabe Medical Frontier Conference, the Ube Research Foundation, the Yamanouchi Foundation for Research on Metabolic Disorders, and a Precursory Research for Embryonic Science and Technology investigatorship from the Japan Science and Technology Corporation (to H.B.). T.F. is a recipient of a pre- and postdoctoral fellowship from the Japan Society for the Promotion of Science.

1. Andersen, P. (1999) *Nature* **399**, 19–21.
2. Smith, S. J. (1999) *Science* **283**, 1860–1861.
3. Blackstone, C. & Sheng, M. (1999) *Cell Calcium* **26**, 181–192.
4. Bliss, T. V. & Collingridge, G. L. (1993) *Nature* **361**, 31–39.
5. Kennedy, M. B. (1998) *Brain Res. Brain Res. Rev.* **26**, 243–257.
6. Kim, J. H. & Huganir, R. L. (1999) *Curr. Opin. Cell Biol.* **11**, 248–254.
7. Ziff, E. B. (1997) *Neuron* **19**, 1163–1174.
8. Friedman, H. V., Bresler, T., Garner, C. C. & Ziv, N. E. (2000) *Neuron* **27**, 57–69.
9. Andersen, P. & Soleng, A. F. (1998) *Brain Res. Brain Res. Rev.* **26**, 353–359.
10. Dalva, M. B., Ghosh, A. & Shatz, C. J. (1994) *J. Neurosci.* **14**, 3588–3602.
11. Engert, F. & Bonhoeffer, T. (1999) *Nature* **399**, 66–70.
12. Hosokawa, T., Rusakov, D. A., Bliss, T. V. & Fine, A. (1995) *J. Neurosci.* **15**, 5560–5573.
13. Kirov, S. A. & Harris, K. M. (1999) *Nat. Neurosci.* **2**, 878–883.
14. Maletic-Savatic, M., Malinow, R. & Svoboda, K. (1999) *Science* **283**, 1923–1927.
15. Toni, N., Buchs, P. A., Nikonenko, I., Bron, C. R. & Muller, D. (1999) *Nature* **402**, 421–425.
16. Koh, Y. H., Popova, E., Thomas, U., Griffith, L. C. & Budnik, V. (1999) *Cell* **98**, 353–363.
17. Shen, K. & Meyer, T. (1999) *Science* **284**, 162–166.
18. Shi, S. H., Hayashi, Y., Petralia, R. S., Zaman, S. H., Wenthold, R. J., Svoboda, K. & Malinow, R. (1999) *Science* **284**, 1811–1816.
19. Rao, A. & Craig, A. M. (1997) *Neuron* **19**, 801–812.
20. Dunaevsky, A., Tashiro, A., Majewska, A., Mason, C. & Yuste, R. (1999) *Proc. Natl. Acad. Sci. USA* **96**, 13438–13443.
21. Fischer, M., Kaech, S., Knutti, D. & Matus, A. (1998) *Neuron* **20**, 847–854.
22. Allison, D. W., Gelfand, V. I., Spector, I. & Craig, A. M. (1998) *J. Neurosci.* **18**, 2423–2436.
23. Job, C. & Lagnado, L. (1998) *J. Cell Biol.* **143**, 1661–1672.
24. Lau, P. M., Zucker, R. S. & Bentley, D. (1999) *J. Cell Biol.* **145**, 1265–1275.
25. Furukawa, K., Fu, W., Li, Y., Witke, W., Kwiatkowski, D. J. & Mattson, M. P. (1997) *J. Neurosci.* **17**, 8178–8186.
26. Halpain, S., Hipolito, A. & Saffer, L. (1998) *J. Neurosci.* **18**, 9835–9844.
27. Colicos, M. A., Collins, B. E., Sailor, M. J. & Goda, Y. (2001) *Cell* **107**, 605–616.
28. Bito, H., Deisseroth, K. & Tsien, R. W. (1996) *Cell* **87**, 1203–1214.
29. Matus, A., Ackermann, M., Pehling, G., Byers, H. R. & Fujiwara, K. (1982) *Proc. Natl. Acad. Sci. USA* **79**, 7590–7594.
30. Fifkova, E. & Morales, M. (1992) *Int. Rev. Cytol.* **139**, 267–307.
31. Emptage, N., Bliss, T. V. & Fine, A. (1999) *Neuron* **22**, 115–124.
32. Schiller, J., Schiller, Y. & Clapham, D. E. (1998) *Nat. Neurosci.* **1**, 114–118.
33. Yuste, R., Majewska, A., Cash, S. S. & Denk, W. (1999) *J. Neurosci.* **19**, 1976–1987.
34. Somlyo, A. P. & Somlyo, A. V. (1994) *Nature* **372**, 231–236.
35. Hell, J. W., Westenbroek, R. E., Warner, C., Ahlijanian, M. K., Prystay, W., Gilbert, M. M., Snutch, T. P. & Catterall, W. A. (1993) *J. Cell Biol.* **123**, 949–962.

Impaired adrenocorticotropic hormone response to bacterial endotoxin in mice deficient in prostaglandin E receptor EP1 and EP3 subtypes

Yoko Matsuoka*†, Tomoyuki Furuyashiki*, Haruhiko Bito*, Fumitaka Ushikubi*, Yasuhiro Tanaka*, Takuya Kobayashi*, Seiji Muro†, Noriko Satoh†, Tetsuro Kayahara‡, Mikito Higashi‡, Akira Mizoguchi‡, Hitoshi Shichi§, Yoshihiro Fukuda†, Kazuwa Nakao†, and Shuh Narumiya*¶

Departments of *Pharmacology and †Medicine and Clinical Science, Kyoto University Faculty of Medicine, Kyoto 606-8501, Japan; ‡Department of Anatomy, Mie University Faculty of Medicine, Tsu 514-8507, Japan; and §Department of Ophthalmology, Wayne State University School of Medicine, Detroit, MI 48201

Edited by Shigetada Nakanishi, Kyoto University, Kyoto, Japan, and approved February 3, 2003 (received for review June 4, 2002)

Sickness evokes various neural responses, one of which is activation of the hypothalamo–pituitary–adrenal (HPA) axis. This response can be induced experimentally by injection of bacterial lipopolysaccharide (LPS) or inflammatory cytokines such as IL-1. Although prostaglandins (PGs) long have been implicated in LPS-induced HPA axis activation, the mechanism downstream of PGs remained unsettled. By using mice lacking each of the four PGE receptors (EP1–EP4) and an EP1-selective antagonist, ONO-8713, we showed that both EP1 and EP3 are required for adrenocorticotropic hormone release in response to LPS. Analysis of c-Fos expression as a marker for neuronal activity indicated that both EP1 and EP3 contribute to activation of neurons in the paraventricular nucleus of the hypothalamus (PVN). This analysis also revealed that EP1, but not EP3, is involved in LPS-induced activation of the central nucleus of the amygdala. EP1 immunostaining in the PVN revealed its localization at synapses on corticotropin-releasing hormone-containing neurons. These findings suggest that EP1- and EP3-mediated neuronal pathways converge at corticotropin-releasing hormone-containing neurons in the PVN to induce HPA axis activation upon sickness.

During sickness, various responses of the CNS are evoked in animals through the immune–brain interaction, one prominent example being the activation of the hypothalamo–pituitary–adrenal (HPA) axis (1, 2). In this response, a population of parvocellular neurons in the paraventricular nucleus of the hypothalamus (PVN) are activated to secrete corticotropin-releasing hormone (CRH), which then triggers the release of adrenocorticotropic hormone (ACTH) from the pituitary to the plasma, and the latter finally stimulates the secretion of corticosteroids (2). This neuroendocrine cascade is a primordial step in host defense mechanism that is mobilized upon exposure to a large variety of stresses (2–4). Activation of the HPA axis that occurs during systemic diseases can be mimicked experimentally by injection of bacterial endotoxin, lipopolysaccharide (LPS), or inflammatory cytokines such as IL-1. By using these models, the mechanism of the sickness-induced HPA axis activation has been studied extensively, and these studies suggest the involvement of prostaglandins (PGs) in the initiation of this neuroendocrine cascade.

PGs are lipid mediators produced from arachidonic acid by the sequential actions of cyclooxygenases (COX) and respective synthases, and they include PGD_2, PGE_2, $PGF_{2\alpha}$, PGI_2, and thromboxane A_2 (5). They are released from cells in response to a variety of physiological and pathological stimuli and act in the vicinity of their site of synthesis. Roles of PGs have been studied by examining actions of either exogenously applied PGs or nonsteroidal antiinflammatory drugs (NSAIDs), such as indomethacin, that block the production of PGs by inhibiting COX. Indeed, in previous experiments the HPA axis activation by either LPS or IL-1 was attenuated by pretreatment of animals with NSAIDs, and PGE_2 injected centrally into the brain induced PVN activation and ACTH release (6–11). However, the inhibition by NSAIDs was not always complete, was often short-lived, and was sometimes inconsistent (2). In addition, no systematic effort to pinpoint the identity of the critical PG involved in this process has yet been performed. Consequently, the physiological significance of PGs in HPA axis regulation has remained obscure. This situation appears to be mainly because of the lack of appropriate experimental tools to dissect various PG-mediated steps in the CNS.

PGs exert their effects through interaction with eight types and subtypes of cell surface receptors. They include PGD receptor (DP), four subtypes of PGE receptor (EP1, EP2, EP3, and EP4), PGF receptor (FP), PGI receptor (IP), and thromboxane A receptor (TP). All of these receptors are G protein-coupled receptors with seven transmembrane domains (5). We have disrupted genes for these receptors individually in mice and analyzed phenotypes of the resulting knockout animals (12–17). Using these mice, we showed previously that the PGE receptor EP3 in the brain plays a critical role in the generation of febrile response to LPS and IL-1β (15). Because LPS and IL-1 evoke activation of the HPA axis together with fever under these conditions, we suspected that PGE_2–EP3-mediated mechanism also might underlie elicitation of other CNS responses to sickness. Our results suggest that LPS-induced ACTH release indeed is defective in EP3-deficient mice. However, we found that this ACTH response also is defective in EP1-deficient mice. Furthermore, both EP1 and EP3 play a critical role in regulating the PVN in the HPA axis activation.

Materials and Methods

Mice. Mice lacking EP1, EP2, EP3, or EP4 receptor were generated as described (14–16). With the exception of $EP4^{-/-}$ mice, each mutant line was backcrossed for more than five generations into C57BL/6CrSlc (Japan SLC, Hamamatsu, Japan). Because most $EP4^{-/-}$ mice die postnatally (14), survivors of the F_2 progenies of $EP4^{-/-}$ mice in the mixed genetic background of 129/Ola × C57BL/6 were intercrossed and the resultant male survivors were used. All experiments were performed according to the guidelines for animal experiments of Kyoto University.

Measurement of LPS-Induced ACTH Release. Before each experiment, 8- to 12-week-old male mice were caged individually for 3

This paper was submitted directly (Track II) to the PNAS office.

Abbreviations: ACTH, adrenocorticotropic hormone; CeA, central nucleus of the amygdala; COX, cyclooxygenase; CRH, corticotropin-releasing hormone; HPA, hypothalamo–pituitary–adrenal; IR, immunoreactivity; LPS, lipopolysaccharide; mPGES-1, microsomal prostaglandin E synthase; NSAIDs, nonsteroidal antiinflammatory drugs; NTS, nucleus of the solitary tract; PG, prostaglandin; PVN, paraventricular nucleus of the hypothalamus; VLM, ventrolateral medulla.

¶To whom correspondence should be addressed. E-mail: snaru@mfour.med.kyoto-u.ac.jp.

www.pnas.org/cgi/doi/10.1073/pnas.0633341100

days under standard conditions (12-h light/12-h dark cycle; light on between 0900 and 2100), with free access to chow and water, and handled daily. Each mouse was injected i.p. with 0.11 ml of an LPS (*Escherichia coli* O26:B6) suspension (0.02 mg/ml) and killed by decapitation. Plasma ACTH concentration was determined with an immunoradiometric assay kit as described (18). A volume of 0.22 ml of indomethacin solution (5 mg/ml in Dulbecco's PBS) or vehicle was injected i.p. 15 min before LPS injection. An EP1 antagonist, ONO-8713 (19), kindly provided by Ono Pharmaceutical (Osaka), was dissolved at a concentration of 10 mg/ml in 1 M NaOH containing 5% glucose. The solution was adjusted to pH 9.0 with 5 M HCl and then diluted 10-fold with PBS before i.p injection of 0.22 ml 60 min before LPS injection.

Immunohistochemistry. For immunostainings of c-Fos and CRH, mice were killed by transcardiac perfusion with 0.1 M phosphate buffer containing 4% paraformaldehyde. Coronal brain sections of 30-μm thickness were prepared, and c-Fos immunoreactivity (Fos-IR) was detected by using a rabbit polyclonal anti-c-Fos antibody (1:2,000 dilution, Ab-5; Oncogene Science) and a Vectastain ABC-PO kit (Vector Laboratories), as described (20). Two sections with the highest numbers of Fos-IR-positive cells were identified for each region, and the mean number was taken as the representative score for each mouse. For double immunostaining, sections were incubated with the anti-c-Fos and guinea pig anti-CRH (1:200 dilution, T-5007; Peninsula Laboratories) antibodies. Signals were detected with Alexa 488-labeled anti-rabbit and Alexa 594-labeled anti-guinea pig IgG antibodies (1:200 dilution; Molecular Probes), respectively.

Immunostaining of COX-1, COX-2, and microsomal PGE synthase-1 (mPGES-1) was carried out as described (21, 22) by using mouse anti-COX-1 (1:500 dilution, 160110; Cayman Chemical, Ann Arbor, MI), goat anti-COX-1 (1:1,000 dilution, sc-1752, Lot D-208; Santa Cruz Biotechnology), rabbit anti-mouse COX-2 (1:1,000 dilution, 160126; Cayman Chemical), rabbit anti-mPGES-1 (1:1,500 dilution, 160140; Cayman Chemical), or guinea pig anti-mPGES-1 (1:500 dilution; ref. 23) antibodies. COX-1-IR was detected by Alexa 488-labeled anti-mouse and/or Alexa 594-labeled anti-goat IgG antibodies (1:500 dilution; Molecular Probes). Signals for COX-2 and mPGES-1 were detected with a biotinylated anti-rabbit IgG antibody (Jackson ImmunoResearch) followed by Alexa 488- or Alexa 594-labeled streptavidin (Molecular Probes) or with Alexa 488-labeled anti-guinea pig IgG antibody. The specificity of each signal was confirmed by the use of two independent antibodies for COX-1 and mPGES-1 or by loss of COX-2-IR on brain sections from COX-2$^{-/-}$ mice.

For immunostaining of EP1, synaptophysin, and CRH, fresh brains were frozen, cut coronally at a thickness of 10 μm, then serially treated with 95% ethanol at −20°C for 30 min and 100% acetone for 3 min at room temperature. They were incubated with rabbit anti-EP1 (1:400 dilution) (24), mouse anti-synaptophysin (1:50 dilution, 61012; Progen, Heidelberg), and/or guinea pig anti-CRH antibodies. Signals were detected with fluorescein- and/or Texas red-labeled secondary antibodies (1:200 dilution). All fluorescent images were acquired with laser-scanning confocal microscopy [MRC1024 (Bio-Rad) or LSM510 (Zeiss)].

Semiquantitative RT-PCR. Mice were injected with LPS (2.5 mg/kg) i.p. and killed by decapitation 3 h later. The hypothalamus was isolated as defined (25) and homogenized within 3 min after decapitation. Total RNA was extracted by using TRIzol solution (Invitrogen) and subjected to semiquantitative RT-PCR by using Light-Cycler (Roche Diagnostics) as described (26). Primers and fluorescent probes for mouse c-fos and GAPDH mRNA were obtained from Nihon Gene Research Laboratories (Sendai, Japan). The amount of c-Fos mRNA was normalized to that of GAPDH mRNA from the same cDNA sample and is shown as the ratio to the value in vehicle-treated wild-type mice.

Statistical Analyses. Data are shown as means ± SEM. Comparison of two groups was analyzed by Student's t test. For comparison of more than two groups with comparable variances, one-way ANOVA was performed first. Then, either Dunnett's or Tukey's test was used to evaluate pairwise group difference. If the variances of the groups were significantly different, a Kruskal–Wallis test followed by Dunn's test was used for nonparametric comparisons. The analyses were performed with the use of PRISM 3.0 software (GraphPad, San Diego).

Results

LPS-Induced HPA Axis Activation Is Impaired in EP1$^{-/-}$ and EP3$^{-/-}$ Mice. Given the previous inconsistent effects of NSAIDs on ACTH release (see ref. 2), we first examined the time course of inhibition of ACTH response to LPS by indomethacin. We measured the plasma ACTH concentration at various times after LPS injection (0.1 mg/kg i.p.) without (vehicle/LPS) or with (IND/LPS) indomethacin administered (50 mg/kg i.p.) 15 min before LPS injection (Fig. 1*A*). The ACTH concentration in the vehicle/LPS group significantly increased at 60 min, peaked at 120 min, and decreased but still remained higher than the control at 180 min, whereas no change was observed in control mice injected with saline. Indomethacin treatment before LPS challenge abolished the ACTH increase at 60 and 180 min. The peak response at 120 min was not affected significantly, although the value at 120 min also tended to be lower than that for the vehicle/LPS group. These results indicate that the LPS-induced ACTH release in mice is composed of two components: an indomethacin-sensitive component that was apparent at all time points and an indomethacin-resistant component that was transient and peaked at 120 min. A similar NSAID effect on LPS-induced ACTH release was reported previously (27).

We next examined whether LPS induces the release of ACTH in mice deficient in any one of the four EP subtypes. The plasma ACTH level from the knockout and wild-type mice was measured at 1 h after LPS challenge. At this time point, EP2$^{-/-}$ and EP4$^{-/-}$ mice exhibited an increase in ACTH concentration similar to that apparent in wild-type mice (Fig. 1*B*). However, no increase in ACTH concentration was found in either EP1$^{-/-}$ or EP3$^{-/-}$ mice. As found in the indomethacin-treated animals, both EP1$^{-/-}$ and EP3$^{-/-}$ mice elicited a peak of ACTH release at 2 h after LPS injection, but neither of them showed the increase at 3 h (data not shown). The impairment in EP1$^{-/-}$ and EP3$^{-/-}$ mice was confirmed by comparing the responses among littermates born from EP1- or EP3-heterozygous mice (data not shown). The role of EP1 in ACTH release was confirmed further pharmacologically by the use of a highly selective EP1 antagonist, ONO-8713 (19) (Fig. 1*C*). The treatment with this antagonist suppressed the LPS-induced ACTH release in wild-type mice, whereas it did not affect the febrile response, an EP3-mediated process (15) (Fig. 1 *D* and *E*). These results suggest that both EP1 and EP3 play a crucial role in mediating LPS-induced ACTH release and, further, that EP1 participates in this response by a process independent of EP3-mediated febrile response.

Defective LPS-Induced c-Fos Expression in Neurons of EP1$^{-/-}$ and EP3$^{-/-}$ Mice. The loss of LPS-induced ACTH release by EP1 or EP3 deficiency described above could be attributed to defect(s) either in PVN activation or in CRH action on the pituitary. To examine which step is affected by EP1 or EP3 deficiency, we determined LPS-induced c-fos expression in the PVN and the pituitary of wild-type, EP1$^{-/-}$, and EP3$^{-/-}$ mice. Because substantial Fos-IR was detected not at 60 min but at 120 min after

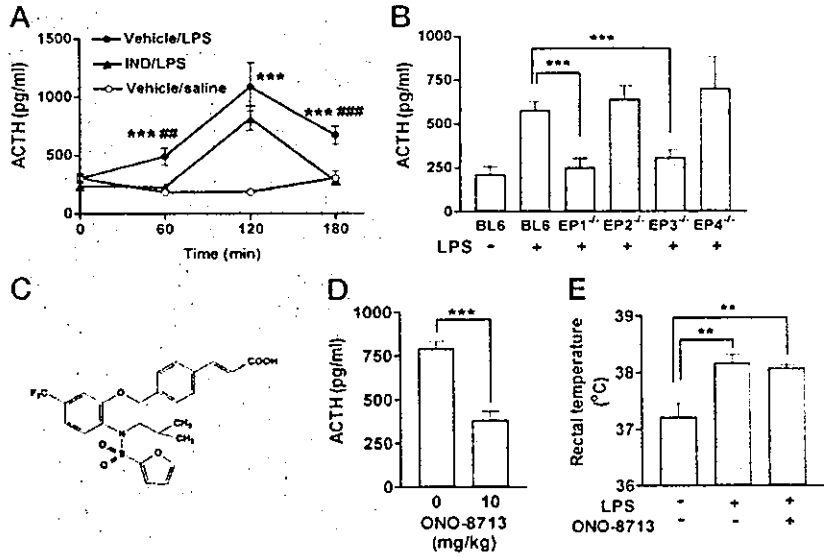

Fig. 1. Impaired LPS-induced ACTH release in $EP1^{-/-}$ and $EP3^{-/-}$ mice. (*A*) Inhibition of LPS-induced ACTH release by indomethacin. Time course of the plasma ACTH concentration after injection of LPS (0.1 mg/kg i.p.) or saline is shown in the absence (Vehicle) or presence (IND) of indomethacin pretreatment (nine mice per group). ○, Vehicle + saline; ●, vehicle + LPS; ▲, indomethacin + LPS. ***, $P < 0.001$ vs. Vehicle/saline; ##, $P < 0.01$; ###, $P < 0.001$ vs. IND/LPS. (*B*) Effects of EP deficiency on LPS-induced ACTH release. Wild-type mice were injected with either saline ($n = 6$) or LPS ($n = 9$). $EP1^{-/-}$ ($n = 9$), $EP2^{-/-}$ ($n = 9$), $EP3^{-/-}$ ($n = 9$), and $EP4^{-/-}$ ($n = 5$) mice were injected with LPS. Their plasma ACTH concentrations were measured after 1 h. ***, $P < 0.001$. (*C*) Structure of ONO-8713. (*D*) Inhibition of LPS-induced ACTH release by ONO-8713 ($n = 6$ each). ***, $P < 0.001$. (*E*) Effect of ONO-8713 on LPS-induced increase in body temperature ($n = 6$ each). **, $P < 0.01$.

LPS injection, the numbers of positive cells were determined at the latter time point. Wild-type, $EP1^{-/-}$, and $EP3^{-/-}$ mice showed similar numbers of Fos-IR-positive cells in the PVN with no significant difference among the groups (Fig. 2*A*). No difference was found, either, in the pituitary among the three lines of mice (data not shown). Although these results appeared to suggest that neither EP1 nor EP3 deficiency affects neuronal activation in these areas, we suspected that either deficiency did affect the activation but only to the level that was sufficient to blunt ACTH release but not sufficient to decrease the number of Fos-IR-positive cells. It is known that the level of c-Fos has a rather complex relationship with neuronal firing (28). Because both EP1 and EP3 are involved in ACTH release, it is possible that inhibition of one of these receptors leaves the pathway

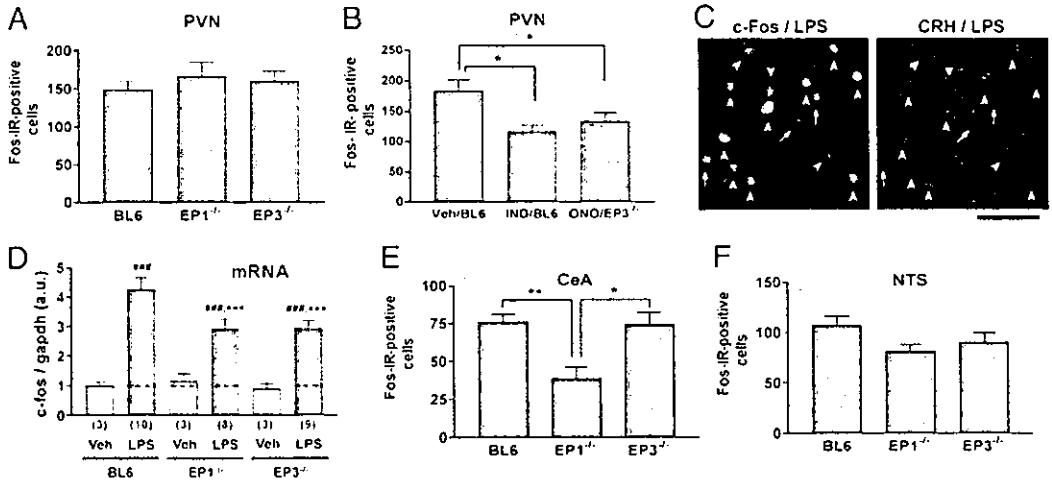

Fig. 2. LPS-induced c-Fos response in wild-type, $EP1^{-/-}$, and $EP3^{-/-}$ mice. (*A*) Fos-IR response in the PVN. The numbers of Fos-IR-positive cells in the PVN of each group of mice are shown ($n = 7$ each). (*B*) Effects of indomethacin and ONO-8713 on Fos-IR response in the PVN. Wild-type mice (BL6) treated with either vehicle (Veh; $n = 7$) or indomethacin (IND; $n = 7$) or $EP3^{-/-}$ mice treated with ONO-8713 (ONO; $n = 9$) were challenged with LPS and analyzed for c-Fos response. *, $P < 0.05$ vs. vehicle-treated wild-type mice. (*C*) Double immunostaining of c-Fos and CRH in the PVN of LPS-treated wild-type mice. Arrowheads and arrows show Fos-IR-positive neurons with or without CRH-IR, respectively. (Bar = 50 μm.) (*D*) Induction of c-fos mRNA. Wild-type (BL6), $EP1^{-/-}$, and $EP3^{-/-}$ mice (the numbers appear in parentheses) were injected with either vehicle or LPS, and c-fos mRNA in the hypothalamus was quantified by RT-PCR. The amount of c-fos mRNA was normalized to that of GAPDH mRNA. ###, $P < 0.001$ vs. vehicle-treated mice of the respective genotype; ***, $P < 0.001$ vs. LPS-treated wild-type mice. (*E*) Fos-IR response in the central nucleus of the amygdala (CeA) ($n = 7$ each). *, $P < 0.05$ and **, $P < 0.01$ vs. $EP3^{-/-}$ and wild-type mice, respectively. (*F*) Fos-IR response in the nucleus of the solitary tract (NTS). The numbers of wild-type, $EP1^{-/-}$, and $EP3^{-/-}$ mice are 13, 14, and 8, respectively.

mediated by the other receptor intact, which may be sufficient for Fos induction. We therefore decided to inhibit all of the PG-mediated pathways by treatment with indomethacin and examine its effects on Fos induction. Indeed, in keeping with previous studies (9, 10), the treatment with indomethacin significantly decreased the number of LPS-induced Fos-IR-positive cells in the PVN (Fig. 2*B*). We therefore administered ONO-8713 to EP3$^{-/-}$ mice to block both EP1 and EP3 in these animals and measured c-Fos expression in the PVN. Intriguingly, treatment of EP3$^{-/-}$ mice with ONO-8713 resulted in a decrease in the number of Fos-IR-positive cells to an extent comparable to that found in indomethacin-treated wild-type mice (Fig. 2*B*). Double immunostaining with c-Fos and CRH antibodies revealed that most c-Fos-positive neurons in the PVN of wild-type mice were CRH-immunoreactive (Fig. 2*C*). Thus, c-Fos reduction in EP3$^{-/-}$ mice with ONO-8713 is likely to occur in CRH-containing neurons in the PVN.

Because the above c-Fos assay measured the number of Fos-IR-positive cells irrespective of its amount in each cell, we next quantified the amount of c-Fos mRNA by RT-PCR. Because of the detection threshold of this method, we treated mice with a high dose of LPS (2.5 mg/kg i.p.) and subjected the whole hypothalamus to the analysis. The LPS injection indeed induced a significant amount of c-Fos mRNA in the hypothalamus, and this induction was impaired in both EP1$^{-/-}$ and EP3$^{-/-}$ mice (Fig. 2*D*). These results strongly suggest that both EP1 and EP3 mediate LPS-induced activation of the hypothalamus. This is consistent with a view that a pathway mediated by either EP1 or EP3 alone can activate neurons in the PVN to some extent, but the synergistic activation by both pathways is required for PVN activation sufficient for ACTH release.

We next extended the Fos-IR analysis to other regions known to be activated in response to LPS in rats (9, 10, 29). They include the central nucleus of the amygdala (CeA), the nucleus of the solitary tract (NTS), and the ventrolateral medulla (VLM). A sizable number of neurons were responsive to LPS in CeA of wild-type mice (Fig. 2*E*). Notably, EP1$^{-/-}$ mice showed a significant reduction in the number of Fos-IR-positive cells (Fig. 2*E*), indicating the involvement of EP1 in LPS-induced activation of CeA neurons. A small decrease in c-Fos expression also was noted in NTS of EP1$^{-/-}$ mice compared with wild-type mice, but the difference was not statistically significant (Fig. 2*F*). No decrease was found in either region of EP3$^{-/-}$ mice. In the VLM, only very sparse c-Fos staining was observed in LPS-treated wild-type mice (data not shown), which precluded quantitative comparison among mice of different genotypes. A similar c-Fos analysis also was performed in EP2$^{-/-}$ and EP4$^{-/-}$ mice. However, no difference was found in any of the above regions of EP2$^{-/-}$ or EP4$^{-/-}$ mice as compared with wild-type or control mice of identical genetic background (data not shown).

EP1 Is Localized at the Synapse on CRH-Containing Neurons in the PVN. The above findings demonstrated that EP1 and EP3 distinctly but synergistically regulate LPS-induced CNS responses. Localization of EP3 in the brain already was studied extensively by both *in situ* hybridization (20, 30, 31) and immunohistochemistry (32). Whereas the former studies detected little hybridization signals for EP3 mRNA in the PVN, the latter study reported moderate EP3-IR in the neuropil in this area, suggesting that EP3 may be present at terminals of neurons projecting to this area. On the other hand, *in situ* hybridization studies of EP1 (20, 33) revealed weak and diffuse signals in the PVN and provide no information on its expression in CeA. No systematic analysis of EP1 immunostaining in the brain is yet available. We therefore examined EP1 expression in these areas by immunohistochemistry using an anti-EP1 antibody (24).

We first verified the specificity of this antibody by using cultured cells expressing cloned EP1 or EP3 receptor. This

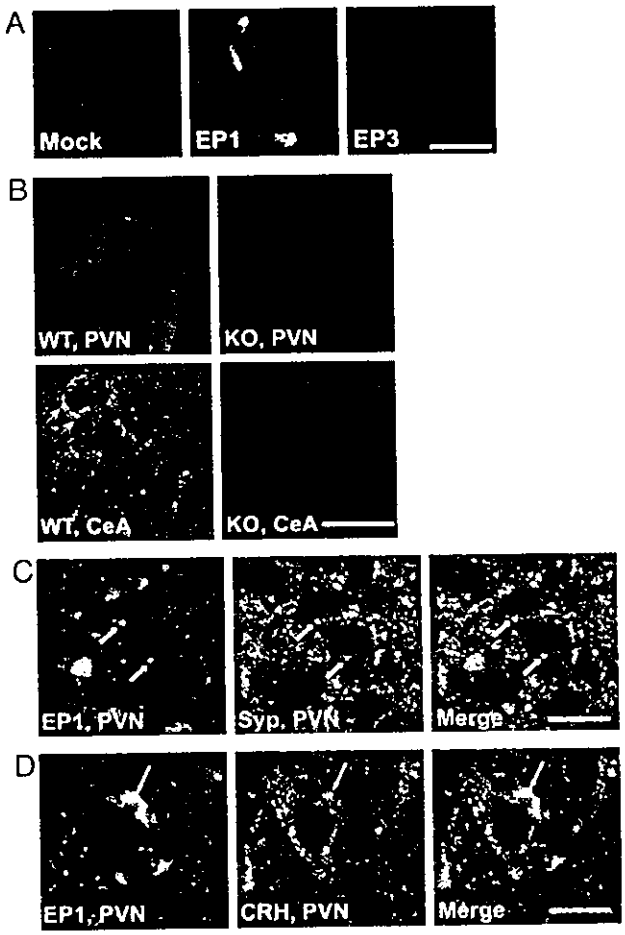

Fig. 3. Localization of EP1 in PVN and CeA. (*A*) Specificity of the antibody. EP1-IR of COS-7 cells expressing LacZ (Mock), EP1, or EP3 is shown. (Bar = 50 μm.) (*B*) EP1-IR in PVN and CeA of wild-type (WT) and EP1$^{-/-}$ (KO) mice. (Bar = 200 μm for PVN and 25 μm for CeA.) (*C*) Double immunostaining of EP1 and synaptophysin (Syp). Arrows show the colocalized signals of EP1-IR and Syp-IR. (Bar = 20 μm.) (*D*) Double immunostaining of EP1 and CRH. (Bar = 10 μm.)

antibody stained COS-7 cells expressing EP1 and not cells transfected with either LacZ or EP3 (Fig. 3*A*). Brain sections then were subjected to staining with this antibody. As shown in Fig. 3*B*, EP1-IR was detected in the PVN and CeA of wild-type mice as punctate signals. On the other hand, little, if any, signal was found in the corresponding brain regions of EP1$^{-/-}$ mice, indicating that the IR detected in wild-type mice represents EP1. Double immunostaining showed that most of EP1-IR puncta in the PVN and CeA were colocalized with those stained for synaptophysin (Fig. 3*C* and data not shown). Furthermore, some, if not all, EP1-IR puncta were clearly juxtaposed with CRH-IR-positive neurons in the PVN (Fig. 3*D*). These data suggest that EP1 is present at the synapses on CRH-containing neurons in the PVN.

Localization of Enzymes in PGE Synthesis. Given the local action of PGs, the site of PGE_2 synthesis is critical to understand where and how EP1 and EP3 are activated. We therefore examined the localization of enzymes responsible for PGE_2 synthesis, namely, COX-1, COX-2, and mPGES-1, in the PVN by immunohistochemistry. As reported (21), COX-1-IR was expressed constitutively on glia-like cells in the PVN (Fig. 4) as well as other brain

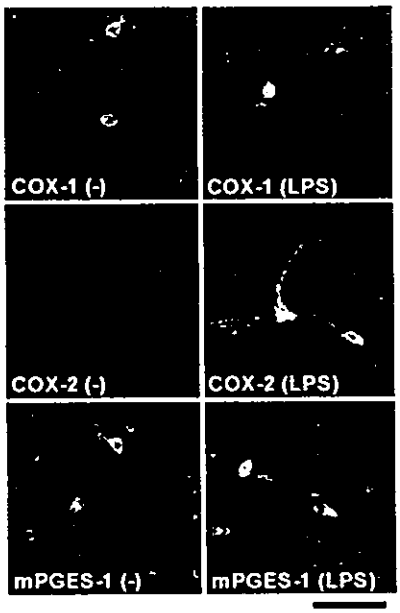

Fig. 4. Localization of enzymes for PGE_2 synthesis in the PVN. Wild-type mice were treated with or without LPS, and the brain was isolated and subjected to the analysis 3 h after injection. (Bar = 30 μm.)

areas (data not shown) of mice with or without LPS. In contrast, COX-2-IR was inducible and was detectable in the PVN only at 3 h, but not at 1 h, after LPS challenge as a pattern reminiscent of blood vessels (Fig. 4 and data not shown). mPGES-1 also was stained in the vessel-like structure within the PVN, but the level of its expression appeared unaltered with or without LPS challenge (Fig. 4). This constitutive expression of mPGES-1 was in contrast to the previous reports that it is induced by LPS challenge (22, 34). The specificity of this mPGES-1-IR was confirmed by using two independent mPGES-1 antibodies, which yielded overlapped staining patterns (data not shown).

Discussion

A role of PGs in the HPA axis activation induced by LPS or inflammatory cytokines has long been suggested (6–11). However, the importance and identity of the PG-mediated process in this response have remained to be examined (2). This is probably because pharmacological effects of NSAIDs were variable and because specific drugs for each PG receptor subtype were not available. With the use of knockout mice deficient in each of the four PGE receptor subtypes, we showed that LPS-induced ACTH release was impaired in mice deficient in either EP1 or EP3 but not in those lacking either EP2 or EP4 (Fig. 1). This study thus unambiguously demonstrated the direct involvement of PGE_2 in LPS-induced HPA axis activation. Given the specific involvement of EP3 but not EP1 in LPS-induced fever generation (15), this study further suggests that at least some PG-mediated mechanisms are different in fever generation and ACTH release induced by LPS. Our findings appear contradictory to the current proposal that EP4 may be a primary PGE receptor mediating the HPA axis activation (35). This proposal is based on the findings that LPS injection induces EP4 in CRH-containing neurons in rat PVN (20, 35). Our results, together with the finding that the EP4 induction is sensitive to NSAID treatment (35), suggest that the EP4 induction is secondary to other PG-mediated processes.

Given the primary role of EP1 and EP3 in ACTH release, we further addressed the site at which EP1 and EP3 act in the HPA axis. The PVN and the pituitary are two critical sites regulating the HPA axis. By using c-Fos as a marker for neuronal activation, we showed that EP1- and EP3-mediated pathways are likely to converge onto the PVN (Fig. 2), although our study did not rule out their involvement in the pituitary. Given that a PG-dependent component of ACTH release is abolished in both $EP1^{-/-}$ and $EP3^{-/-}$ mice (Fig. 1), the synergistic action of EP1 and EP3 appears to be required for PVN activation for ACTH release at least under our experimental conditions. However, we do not exclude a possibility that these two pathways may work differently in time and/or in response to different doses of LPS.

Then, what are the neuronal substrates for the EP1- and EP3-mediated PVN activation? There are multiple brain areas that could regulate the PVN directly or indirectly (36). Forebrain limbic areas, including ventral subiculum, prefrontal cortex, and CeA, are thought to regulate the PVN through intermediate areas such as the bed nucleus of stria terminalis, the preoptic area, and other hypothalamic nuclei. In parallel, the medullary catecholaminergic cell groups such as the VLM directly project to and activate the PVN. Our c-Fos study (Fig. 2) revealed that the number of LPS-induced Fos-IR-positive cells was diminished in CeA of $EP1^{-/-}$ mice, thus implicating the EP1 action in regulating CeA neurons. Consistently, EP1-IR was detected at synapses on CeA neurons (data not shown). On the other hand, the preoptic area and the VLM are possible sites of the EP3 action, because they express EP3 (30–32) and have been suggested to be involved in PGE-mediated HPA axis activation (7, 9, 10, 37). In addition to the PVN activation from other areas, it is also possible that PGs act within the PVN. Indeed, both EP1 and EP3 are distributed in the neuropil of the PVN (Fig. 3 and ref. 32).

Then, what is the cellular mechanism of EPs to activate PVN neurons? Our immunostaining revealed that EP1-IR is localized at the synapse on PVN and CeA neurons (Fig. 3 and data not shown). This finding implicates EP1 in direct regulation of synaptic transmission in the PVN and CeA. It is also reported that EP3 regulates γ-aminobutyrate (GABA)ergic synaptic transmission by a presynaptic mechanism in the supraoptic nucleus (38). GABAergic inputs from similar areas are also found on neurons in the PVN (39). Therefore, EP1 and EP3, which are expressed in neurons, may directly regulate synaptic connections that serve for HPA axis activation. EP1 is present at only a small population of synapses on CRH-containing neurons in the PVN, indicating that EP1 regulates a distinct type of synaptic inputs to CRH-containing neurons. The origin of these projections remains to be clarified.

PGs are formed locally and act in the vicinity of their synthesis (5). It generally is believed that PG synthesis in response to LPS or inflammatory cytokines is catalyzed by COX-2 and mPGES-1 induced in brain vasculature (22, 34). We examined this issue in the PVN and confirmed that COX-2 is induced and coexpressed with mPGES-1 in brain vasculature at 3 h after injection of LPS (Fig. 4), although we found that mPGES-1 is constitutively expressed without LPS stimulation. It is possible that these enzymes catalyze the formation of PGE_2 in the PVN. It was reported previously that PGE_2 is produced significantly in the PVN upon IL-1β injection (40). However, induction of COX-2 in endothelial cells was not observed as early as 1 h after the injection. On the other hand, we observed constitutive expression of COX-1 in glia-like cells in the PVN. There are several reports indicating the involvement of glia in PG production in the brain. Microglial cells produce a large amount of PGs when incubated with LPS *in vitro* (41). PG synthesis associated with neuronal activation also was reported in astrocytes (42). Furthermore, COX-2 is constitutively expressed and localized to the somatodendritic region of excitatory neurons in the cerebral

cortex, the hippocampus (including subiculum), and the amygdala (43, 44), all of which may contribute to HPA axis activation (36). Therefore, it is possible that multiple pathways for PG synthesis, each of which is activated in a different temporal pattern in response to LPS, contribute to PG-mediated HPA axis activation.

In summary, we demonstrated that two distinct pathways mediated by EP1 and EP3 are activated in response to LPS and are required for LPS-induced PVN activation in the HPA axis. This knowledge will help further clarify novel neural mechanisms implicated in sickness-induced CNS symptoms.

We thank A. Shimatsu, Y. Sugimoto, and E. Segi for helpful discussions and comments, K. Matsumura for advice on the immunohistochemistry of COX-1, COX-2, and mPGES-1, N. Eguchi for a guinea pig anti-mPGES-1 antibody, C. Hamada for advice on statistical analyses, K. Deguchi, N. Kitagawa, and T. Fujiwara for animal care and breeding, and T. Arai and H. Nose for secretarial assistance. This work was supported in part by Grants-in-Aid for Scientific Research from the Ministry of Education, Science, Sports and Culture of Japan and by grants from the Organization for Pharmaceutical Safety and Research of Japan, the Mitsubishi Foundation, and the ONO Medical Research Foundation. T.F. is a postdoctoral fellow of the Japan Society for the Promotion of Science.

1. Kent, S., Bluthé, R.-M., Kelley, K. W. & Dantzer, R. (1992) *Trends Pharmacol. Sci.* **13**, 24–28.
2. Turnbull, A. V. & Rivier, C. L. (1999) *Physiol. Rev.* **79**, 1–71.
3. Kopin, I. J. (1995) *Ann. N.Y. Acad. Sci.* **771**, 19–30.
4. Johnson, E. O., Kamilaris, T. C., Chrousos, G. P. & Gold, P. W. (1992) *Neurosci. Biobehav. Rev.* **16**, 115–130.
5. Narumiya, S., Sugimoto, Y. & Ushikubi, F. (1999) *Physiol. Rev.* **79**, 1193–1226.
6. Morimoto, A., Murakami, N., Nakamori, T., Sakata, Y. & Watanabe, T. (1989) *J. Physiol. (London)* **411**, 245–256.
7. Katsuura, G., Arimura, A., Koves, K. & Gottschall, P. E. (1990) *Am. J. Physiol.* **258**, 163–171.
8. Rivier, C. & Vale, W. (1991) *Endocrinology* **129**, 384–388.
9. Lacroix, S. & Rivest, S. (1997) *J. Comp. Neurol.* **387**, 307–324.
10. Ericsson, A., Arias, C. & Sawchenko, P. E. (1997) *J. Neurosci.* **15**, 7166–7179.
11. Nasushita, R., Watanobe, H. & Takebe, K. (1997) *Prostaglandins Leukotrienes Essent. Fatty Acids* **56**, 165–168.
12. Murata, T., Ushikubi, F., Matsuoka, T., Hirata, M., Yamasaki, A., Sugimoto, Y., Ichikawa, A., Aze, Y., Tanaka, T., Yoshida, N., *et al.* (1997) *Nature* **388**, 678–682.
13. Sugimoto, Y., Yamasaki, A., Segi, E., Tsuboi, K., Aze, Y., Nishimura, T., Oida, H., Yoshida, N., Tanaka, T., Katsuyama, M., *et al.* (1997) *Science* **277**, 681–683.
14. Segi, E., Sugimoto, Y., Yamasaki, A., Aze, Y., Oida, H., Nishimura, T., Murata, T., Matsuoka, T., Ushikubi, F., Hirose, M., *et al.* (1998) *Biochem. Biophys. Res. Commun.* **246**, 7–12.
15. Ushikubi, F., Segi, E., Sugimoto, Y., Murata, T., Matsuoka, T., Kobayashi, T., Hizaki, H., Tuboi, K., Katsuyama, M., Ichikawa, A., *et al.* (1998) *Nature* **395**, 281–284.
16. Hizaki, H., Segi, E., Sugimoto, Y., Hirose, M., Saji, T., Ushikubi, F., Matsuoka, T., Noda, Y., Tanaka, T., Yoshida, N., *et al.* (1999) *Proc. Natl. Acad. Sci. USA* **96**, 10501–10506.
17. Matsuoka, T., Hirata, M., Tanaka, H., Takahashi, Y., Murata, T., Kabashima, K., Sugimoto, Y., Kobayashi, T., Ushikubi, F., Aze, Y., *et al.* (2000) *Science* **287**, 2013–2017.
18. Takao, T., Nakata, H., Tojo, C., Kurokawa, H., Nishioka, T., Hashimoto, K. & De Souza, E. (1994) *Brain Res.* **649**, 265–270.
19. Watanabe, K., Kawamori, T., Nakatsuji, S., Ohta, T., Ohuchida, S., Yamamoto, H., Maruyama, T., Kondo, K., Ushikubi, F., Narumiya, S., *et al.* (2000) *Cancer Lett.* **156**, 57–61.
20. Oka, T., Oka, K., Scammell, T. E., Lee, C., Kelly, J. F., Nantel, F., Elmquist, J. E. & Saper, C. B. (2000) *J. Comp. Neurol.* **428**, 20–32.
21. Li, S., Wang, Y., Matsumura, K., Ballou, L. R., Morham, S. G. & Balatteis, C. M. (1999) *Brain Res.* **825**, 86–94.
22. Yamagata, K., Matsumura, K., Inoue, W., Shiraki, T., Suzuki, K., Yasuda, S., Sugiura, H., Cao, C., Watanabe, Y. & Kobayashi, S. (2001) *J. Neurosci.* **21**, 2669–2677.
23. Lazarus, M., Kubata, B. K., Eguchi, N., Fujitani, Y., Urade, Y. & Hayaishi, O. (2002) *Arch. Biochem. Biophys.* **397**, 336–341.
24. Bhattacharya, M., Peri, K. G., Almazan, G., Ribeiro-da-Silva, A., Shichi, H., Durocher, Y., Abramovitz, M., Hou, X., Varma, D. R. & Chemtob, S. (1998) *Proc. Natl. Acad. Sci. USA* **95**, 15792–15797.
25. Calogero, A. E., Gallucci, W. T., Kling, M. A., Chrousos, G. P. & Gold, P. W. (1989) *Brain Res.* **505**, 7–11.
26. Fujiwaki, R., Hata, K., Nakayama, K., Moriyama, M., Iwanari, O., Katabuchi, H., Okamura, H., Sakai, E. & Miyazaki, K. (2002) *Int. J. Cancer* **99**, 328–335.
27. Rivier, C. (1994) in *Bilateral Communication Between the Endocrine and Immune Systems*, ed. Grossman, C. (Springer, New York), Vol. 7, pp. 183–196.
28. Shin, C., McNamara, J. O., Morgan, J. I., Curran, T. & Cohen, D. R. (1990) *J. Neurochem.* **55**, 1050–1055.
29. Elmquist, J. K., Scammell, T. E., Jacobson, C. D. & Saper, C. B. (1996) *J. Comp. Neurol.* **371**, 85–103.
30. Sugimoto, Y., Shigemoto, R., Namba, T., Negishi, M., Mizuno, N., Narumiya, S. & Ichikawa, A. (1994) *Neuroscience* **62**, 919–928.
31. Ek, M., Arias, C., Sawchenko, P. & Ericsson-Dahlstrand, A. (2000) *J. Comp. Neurol.* **428**, 5–20.
32. Nakamura, K., Kaneko, T., Yamashita, Y., Hasegawa, H., Katoh, H. & Negishi, M. (2000) *J. Comp. Neurol.* **421**, 543–569.
33. Batshake, B., Nilsson, C. & Sundelin, J. (1995) *Eur. J. Biochem.* **231**, 809–814.
34. Ek, M., Engblom, D., Saha, S., Blomqvist, A., Jakobsson, P. & Ericsson-Dahlstrand, A. (2001) *Nature* **410**, 430–431.
35. Zhang, J. & Rivest, S. (2000) *J. Neurochem.* **74**, 2134–2145.
36. Herman, J. P. & Cullinan, W. E. (1997) *Trends Neurosci.* **20**, 78–84.
37. Scammell, T. E., Elmquist, J. K., Griffin, J. D. & Saper, C. B. (1996) *J. Neurosci.* **16**, 6246–6254.
38. Shibuya, I., Setiadji, S. V., Ibrahim, N., Harayama, N., Maruyama, T., Ueta, Y. & Yamashita, H. (2002) *J. Neuroendocrinol.* **14**, 64–72.
39. Armstrong, W. E. (1995) in *The Rat Nervous System*, ed. Paxinos, G. (Academic, San Diego), 2nd Ed., pp. 377–390.
40. Watanobe, H. & Takebe, K. (1994) *Neuroendocrinology* **60**, 8–15.
41. Minghetti, L. & Levi, G. (1998) *Prog. Neurobiol.* **54**, 99–125.
42. Bezzi, P., Carmingnoto, G., Pasti, L., Vesce, S., Rossi, D., Lodi Rizzini, B., Pozzan, T. & Volterra, A. (1998) *Nature* **391**, 281–285.
43. Breder, C. D., Dewitt, D. & Kraig, R. P. (1995) *J. Comp. Neurol.* **355**, 296–315.
44. Kaufmann, W. E., Worley, P. F., Pegg, J., Bremer, M. & Isakson, P. (1996) *Proc. Natl. Acad. Sci. USA* **93**, 2317–2321.

Developmental Cell, Vol. 4, 549–560, April, 2003, Copyright ©2003 by Cell Press

Phosphorylation by Aurora B Converts MgcRacGAP to a RhoGAP during Cytokinesis

Yukinori Minoshima,[1,2] Toshiyuki Kawashima,[1] Koichi Hirose,[1,3] Yukio Tonozuka,[1,2] Aie Kawajiri,[4] Ying Chun Bao,[1,2] Xingming Deng,[5] Masaaki Tatsuka,[6] Shuh Narumiya,[7] W. Stratford May, Jr.,[5] Tetsuya Nosaka,[1] Kentaro Semba,[8] Takafumi Inoue,[9] Takaya Satoh,[10] Masaki Inagaki,[4] and Toshio Kitamura[1,2,*]

[1]Division of Hematopoietic Factors
[2]Division of Cellular Therapy
The Institute of Medical Science
University of Tokyo
Minato-ku
Tokyo 108-8639
Japan
[3]Department of Internal Medicine II
Chiba University School of Medicine
Chiba 260-0856
Japan
[4]Laboratory of Biochemistry
Aichi Center Cancer Research Institute
Nagoya 464-8681
Japan
[5]Shands Cancer Center
University of Florida
Gainesville, Florida 32610
[6]Department of Regulatory Radiobiology
Research Institute for Radiation Biology and Medicine
Hiroshima University
Hiroshima 734-8553
Japan
[7]Department of Pharmacology
Kyoto University Faculty of Medicine
Sakyo-ku
Kyoto 606-8315
Japan
[8]Department of Cellular and Molecular Biology
[9]Division of Molecular Neurobiology
The Institute of Medical Science
University of Tokyo
Minato-ku
Tokyo 108-8639
Japan
[10]Division of Molecular Biology
Department of Molecular and Cellular Biology
Kobe University Graduate School of Medicine
Kobe 650-0017
Japan

Summary

Cell division is finely controlled by various molecules including small G proteins and kinases/phosphatases. Among these, Aurora B, RhoA, and the GAP MgcRacGAP have been implicated in cytokinesis, but their underlying mechanisms of action have remained unclear. Here, we show that MgcRacGAP colocalizes with Aurora B and RhoA, but not Rac1/Cdc42, at the midbody. We also report that Aurora B phosphorylates MgcRacGAP on serine residues and that this modification induces latent GAP activity toward RhoA in vitro. Expression of a kinase-defective mutant of Aurora B disrupts cytokinesis and inhibits phosphorylation of MgcRacGAP at Ser387, but not its localization to the midbody. Overexpression of a phosphorylation-deficient MgcRacGAP-S387A mutant, but not phosphorylation-mimic MgcRacGAP-S387D mutant, arrests cytokinesis at a late stage and induces polyploidy. Together, these findings indicate that during cytokinesis, MgcRacGAP, previously known as a GAP for Rac/Cdc42, is functionally converted to a RhoGAP through phosphorylation by Aurora B.

*Correspondence: kitamura@ims.u-tokyo.ac.jp

Introduction

The small GTPase Rho is known to play important roles in various cellular functions such as stress fiber formation, transcriptional activation, cell motility, and cytokinesis (Hall, 1998). RhoA localizes in the cleavage furrow during cytokinesis and plays critical roles in cytokinesis (Drechsel et al., 1997; Kishi et al., 1993; Mabuchi et al., 1993; Takaishi et al., 1994). In *Xenopus* eggs, microinjection of either the Rho-specific inhibitor C3, an exoenzyme from *Clostridium botulinum*, or a constitutively active mutant $RhoA^{G14V}$ prevents the progression of cytokinesis (Drechsel et al., 1997; Kishi et al., 1993). These data suggested that coordinated cycles of Rho between the active GTP-bound form and the inactive GDP-bound form are indispensable for the completion of cytokinesis. Several GEFs that activate Rho family proteins have been implicated in cytokinesis. One of these GEFs, ECT2, colocalizes with the mitotic spindle in metaphase, transfers to the midzone in anaphase and telophase, and moves to the midbody in cytokinesis (Tatsumoto et al., 1999). It was suggested that accumulation of the active form of RhoA during cytokinesis depended on ECT2 (Kimura et al., 2000). Intriguingly, ECT2 required phosphorylation to exert GDP-GTP exchange activity toward RhoA, Rac1, and Cdc42 (Tatsumoto et al., 1999). On the other hand, it was unclear which RhoGAPs are involved in cytokinesis and how such RhoGAPs are regulated.

We recently identified a GTPase activating protein (GAP), MgcRacGAP, that is essential for cytokinesis in mammals (Hirose et al., 2001). MgcRacGAP colocalizes with the mitotic spindle in metaphase, transfers to the midzone in anaphase, and accumulates to the midbody in cytokinesis. MgcRacGAP associated with tubulin microtubules through its N-terminal myosin-like domain, and overexpression of the N-terminal domain deletion mutant or a GAP activity-defective mutant of MgcRacGAP halted cell division and led to the formation of multinucleated cells (Hirose et al., 2001). It was also reported that CYK-4, a *C. elegans* ortholog of MgcRacGAP, localized to the central spindle, and cytokinesis

was impaired with the defect of central spindle assembly by the mutant *cyk-4* (t1689ts) that carried a mutation at the N terminus (Jantsch-Plunger et al., 2000). Gene depletion of MgcRacGAP in mice leads to death during preimplantation development as a result of impaired mitosis and cytokinesis with binucleated blastomeres in which the nuclei were partially interconnected (Van de Putte et al., 2001). Thus, available data suggest that MgcRacGAP may play an essential role in cytokinesis by association with microtubules. Some investigators reported that CYK-4/MgcRacGAP exerted GAP activities not only toward Rac1 and Cdc42 but also toward RhoA, albeit to a much weaker extent (Jantsch-Plunger et al., 2000; Toure et al., 1998). However, in contrast to their report, we did not detect any GAP activity of MgcRacGAP on RhoA (Kawashima et al., 2000). Raymond et al. also reported that RotundRacGAP, a homolog of mammalian MgcRacGAP in *Drosophila*, possessed no GAP activity toward RhoA (Raymond et al., 2001). Thus, MgcRacGAP does not seem to have an efficient GAP activity toward RhoA if any, and it has remained unclear which small GTPase is the target of MgcRacGAP in cytokinesis.

One of the RasGEFs, Ras-GRF1/CDC25 (Mm), exerts its latent Rac-GEF activity through its tyrosine phosphorylation (Kiyono et al., 2000), and RhoGEF ECT2 requires phosphorylation to exert the exchange activity. In this paper, we demonstrate that Aurora B phosphorylates MgcRacGAP in the midbody, thereby inducing its latent GAP activity toward RhoA during mitosis, and that MgcRacGAP associated with RhoA on the contractile ring. We also identified a serine residue of MgcRacGAP, phosphorylation of which is at least partly responsible for its RhoGAP activity and critical for the completion of cytokinesis.

Results

MgcRacGAP Phosphorylation Occurs in the Midbody during Cytokinesis

MgcRacGAP is located in the midbody during mitosis and plays a critical role in the completion of cytokinesis (Hirose et al., 2001). Curiously, we did not detect a significant GAP activity toward RhoA (Kawashima et al., 2000), although coordinated activation and inactivation of RhoA are known to play critical roles in the completion of cytokinesis. Therefore, we speculated that MgcRacGAP may be modified in the midbody and that its target specificity is changed with this modification.

To characterize the MgcRacGAP protein in the midbody, midbodies were purified from HeLa cells (Mullins and McIntosh, 1982). MgcRacGAP from purified midbodies showed a slower migration than that in the total cell lysate (Figure 1A, lanes 1 and 4). The slow-migrating MgcRacGAP observed in the lysate from purified midbodies showed a partial shift back to the original position by treatment with tyrosine/serine/threonine phosphatase VHR (VH1-related human protein; Figure 1A, lane 2), and this effect was prevented by a protein phosphatase inhibitor, sodium vanadate (Figure 1A, lane 3). The slowly migrating form was not detected using an anti-phosphotyrosine antibody (Ab) 4G10 (data not shown), suggesting that MgcRacGAP was phosphorylated on the

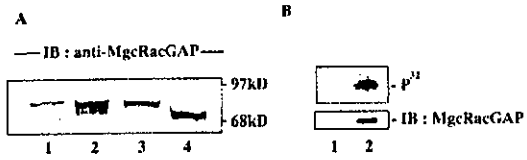

Figure 1. Phosphorylation of MgcRacGAP at the Midbody in Cytokinesis

(A) Slower mobilization of MgcRacGAP in the midbody. The lysate of purified midbodies was separated by SDS-PAGE and immunoblotted with the anti-MgcRacGAP antibody (Ab). MgcRacGAP protein in the lysate from purified midbodies (lane 1) showed slower migration than that in the total cell lysate (lane 4). Lysates from purified midbodies were incubated with the phosphatase VHR in the absence (lane 2) or presence (lane 3) of the phosphatase inhibitor Na_3VO_4 followed by SDS-PAGE.

(B) MgcRacGAP was phosphorylated in the midbody. HeLa cells were metabolically labeled with ^{32}P-labeled orthophosphoric acid. The midbodies were purified, and lysed in a detergent buffer. The lysates were immunoprecipitated with the anti-MgcRacGAP Ab or a control, nonspecific rabbit IgG, and subjected to SDS-PAGE, transferred to a nitrocellulose membrane, and exposed to an X-ray film for 24 hr (upper panel). The same filters were probed by Western blot analysis with the anti-MgcRacGAP Ab (lower panel).

serine/threonine residue(s). To further confirm the phosphorylation, we did ^{32}P-biolabeling of HeLa cells. Indeed, MgcRacGAP incorporated phosphate in the purified midbodies (Figure 1B). These results indicated that MgcRacGAP was phosphorylated in the midbody during cytokinesis.

MgcRacGAP Associates with Aurora B during M Phase and Colocalizes with Aurora B in the Midzone and Midbody

Next, we determined the kinase responsible for the phosphorylation of MgcRacGAP in mitosis. Aurora B/AIM-1 protein localizes at the midbody during telophase and cytokinesis and plays a crucial role in cytokinesis (Terada et al., 1998). Because the localization pattern of Aurora B/AIM-1 and its role in cytokinesis seemed to be similar to those of MgcRacGAP, we reasoned that among various midbody-localized protein kinases, Aurora B was the most likely candidate. To determine whether MgcRacGAP and Aurora B associate with each other during M phase, coimmunoprecipitation studies were done using HeLa cells synchronized as described in Experimental Procedures. Cells at 0, 45, 90, and 180 min after the release from nocodazole treatment were collected. Based on morphological examination and staining with anti-α-tubulin antibody, the cells collected at 0, 45, 90, and 180 min were found to represent cells in prometaphase, metaphase-anaphase, telophase-cytokinesis, and G_1 phase, respectively (data not shown). The cell lysates were immunoprecipitated using an anti-AIM-1/Aurora B monoclonal antibody (mAb) followed by immunoblotting with the anti-MgcRacGAP Ab, and vice versa. A significant amount of MgcRacGAP was detected in the Aurora B immunoprecipitants from the cell lysate prepared at 45 and 90 min, but not at 0 or 180 min (Figure 2A, left upper panel). Consistent with the result shown in Figure 1A, MgcRacGAP protein that was

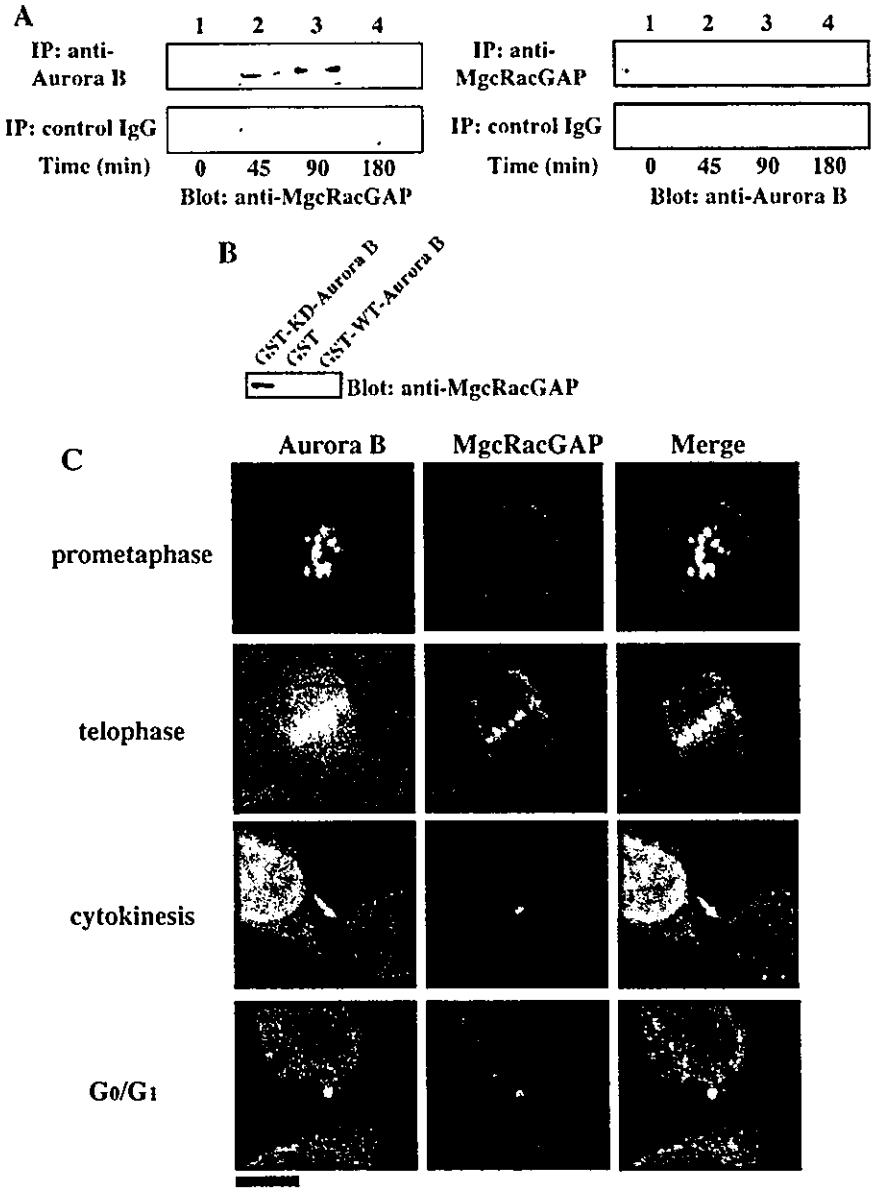

Figure 2. Aurora B Associated with MgcRacGAP during Mitosis

(A) MgcRacGAP associated with Aurora B during M phase. Coimmunoprecipitation experiments were done using synchronized HeLa cells. Cells were collected at 0, 45, 90, and 180 min after nocodazole release. Each sample was subjected to immunoprecipitation using the anti-Aurora B mAb or isotype control Ab followed by immunoblotting with the anti-MgcRacGAP Ab, and vice versa. A significant amount of MgcRacGAP was detected in the Aurora B immunoprecipitants from the cell lysate prepared at 45 or 90 min (left upper panel, lanes 2 and 3) but not in those prepared at 0 or 180 min (left upper panel, lanes 1 and 4). No significant band for MgcRacGAP was detected in the immunoprecipitants of the control Ab at any time indicated (left lower panel). Conversely, a significant amount of Aurora B was detected in the MgcRacGAP immunoprecipitants from the cell lysate prepared at 45 or 90 min (right upper panel, lanes 2 and 3) but not in those prepared at 0 or 180 min (right upper panel, lanes 1 and 4). No significant band for MgcRacGAP was detected in immunoprecipitants of the control Ab at any time indicated (right lower panel).

(B) The association between MgcRacGAP and Aurora B is direct. The same amount (1 μg) of purified MBP-fused MgcRacGAP and GST-fused WT-Aurora B, KD-Aurora B, or GST alone were mixed. Then, GST-WT-Aurora B, GST-KD-Aurora B, or GST alone was recovered with GST beads. The precipitates were probed by Western blot analysis with the anti-MgcRacGAP Ab.

(C) MgcRacGAP colocalized with Aurora B during M phase in the midzone and midbody. Using HeLa cells, immunostaining for Aurora B and MgcRacGAP was done, and cells in the indicated phases of the cell cycle were observed. The immunostained coverslip was viewed using an FLUOVIEW FV300 confocal microscope (Olympus). The scale bar represents 10 μm.

coimmunoprecipitated with Aurora B at 90 min showed a slower migration when compared with that at 45 min, which was presumably due to the phosphorylation of MgcRacGAP. Conversely, a significant amount of Aurora B was also detected in the MgcRacGAP immunoprecipitants from the cell lysate prepared at 45 and 90 min, but not at 0 or 180 min (Figure 2A, right upper panel). These results indicate that Aurora B associates with MgcRacGAP along with the progression of M phase and induces phosphorylation during telophase to cytokinesis.

To determine whether MgcRacGAP and Aurora B are competent to interact in the absence of other mammalian proteins, we did a GST pull-down assay. As shown in Figure 2B, the KD-Aurora B pulled down MBP-fused MgcRacGAP proteins in a higher yield than the WT-Aurora B did, whereas GST alone did not do so. These results indicate that the interaction between MgcRacGAP and Aurora B is direct. We also confirmed the association between Aurora B and MgcRacGAP using confocal microscopy after immunostaining. From anaphase to telophase, Aurora B and MgcRacGAP formed a distinct fine band extending across the midzone and partly colocalized with each other (Figure 2C). During cytokinesis, some fraction of Aurora B condensed to the midbody equator, which is also called the central, dense matrix zone of the midbody, and colocalized with MgcRacGAP. After cytokinesis, both Aurora B and MgcRacGAP remained in the division remnant. These results also suggested that MgcRacGAP was a substrate of Aurora B during mitosis.

Aurora B Directly Phosphorylates MgcRacGAP In Vitro

We did an in vitro kinase assay using the WT or KD mutant of Aurora B against MBP-fusion MgcRacGAP protein and found that the MgcRacGAP protein was phosphorylated by the WT-Aurora B but not by the KD mutant (Figure 3A). Histone H3 protein or MBP served as a positive control (Hsu et al., 2000) or a negative control, respectively. Next, we tested which domains of MgcRacGAP were phosphorylated by Aurora B, and for this we used constructs encoding fusion proteins between MBP and each domain of MgcRacGAP (Figure 3B). We observed that the Internal (*Int*), cystein-rich (*Cys*), and *GAP* domains of MgcRacGAP were phosphorylated by the WT-Aurora B but not by the KD mutant (Figure 3C), suggesting that MgcRacGAP harbored multiple phosphorylation sites that are phosphorylated by Aurora B.

Aurora B-Phosphorylated MgcRacGAP Harbors Prominent GAP Activity toward RhoA

As shown above, the purified C terminus *GAP* domain (MBP-GAPD) was phosphorylated by Aurora B (Figure 3C). We determined whether this phosphorylation might affect its GAP activities toward RhoA, Rac1, or Cdc42 using the MBP-GAPD incubated with either the WT or KD mutant of Aurora B. A prominent GAP activity toward RhoA was observed in the MBP-GAPD incubated with the WT-Aurora B (Figure 4A), suggesting that the GAP activity of MgcRacGAP toward RhoA was induced via phosphorylation of the C terminus *GAP* domain. On the contrary, the GAP activities of the MBP-GAPD toward Rac1 and Cdc42 were barely if at all affected by Aurora B phosphorylation under these conditions. To our knowledge, this is the first report that a GAP is capable of exerting latent GAP activities as a result of modification by phosphorylation.

Phosphorylation of MgcRacGAP at Ser387 Is Responsible for Altered GAP Activities

To determine which residue of MgcRacGAP may be phosphorylated by Aurora B, phosphoamino acid analysis was performed on MBP-MgcRacGAP phosphorylated by Aurora B in vitro. Phosphorylation of MgcRacGAP was primarily detected at serine, with no threonine and tyrosine residues being detectable (Figure 4B). Considering that phosphorylation of the *GAP* domain of MgcRacGAP resulted in the induction of RhoGAP activity (Figure 4A), we generated seven MBP-fusion mutants containing Asp (D) substitution at each of the seven Ser residues in the conserved *GAP* domain of MgcRacGAP. The rationale was that Asp mutants could mimic the charge conferred by a phosphate. These S-D mutants were designated MBP-S364D, -S387D, -S410D, -S420D, -S454D, -S486D, and -S518D. Using the mutants, we tested MgcRacGAP GTP hydrolysis toward RhoA, Rac1, and Cdc42. Only the MBP-S387D and MBP-S518D proteins, but not the other mutants, exerted detectable levels of GAP activity toward RhoA (Figure 4C). Using seven MBP-fused polypeptides that code ten amino acid sequences surrounding the seven Ser residues, we found that Ser387 and Ser410 were specifically phosphorylated (Figure 4D). Altogether, these results suggested that Ser387 of MgcRacGAP was, at least in part, responsible for exerting its latent GAP activity toward RhoA as a result of Aurora B-modified phosphorylation.

Curiously, the MBP-S387D and -S420D proteins failed to have detectable GAP activity toward either Rac1 (Figure 4E) or Cdc42 (data not shown), whereas the MBP-GAPD incubated with the WT-Aurora B still showed strong GAP activity toward Rac/Cdc42 (Figure 4A). This may be because some of the MBP-GAPD proteins incubated with the WT-Aurora B could have remained unphosphorylated and then may exert some GAP activity toward Rac1 and Cdc42. On the other hand, RhoGAP activity of MBP-S387D was not strong (Figure 4C) when compared to that of the MBP-GAPD phosphorylated by WT-Aurora B. This may be because MgcRacGAP requires phosphorylation of multiple residues, inducing Ser387, for efficient RhoGAP activity. The GAP activities of MBP-S387A, which was assumed to mimic unphosphorylated molecules with the substitution of Ser387 residues by Ala, were not altered (Figures 4C and 4E). These data imply that phosphorylation of MgcRacGAP at Ser387 by Aurora B is a critical switch necessary to convert MgcRacGAP from Rac1/Cdc42 GAP to RhoA GAP during M phase.

MgcRacGAP Colocalizes with RhoA at the Late Stage of Cytokinesis on the Contractile Ring

To determine the target G protein of MgcRacGAP during cell division, we compared localization patterns of small GTPases, Rac1, Cdc42, and RhoA with that of MgcRacGAP. During the late stage of cytokinesis, accumulation

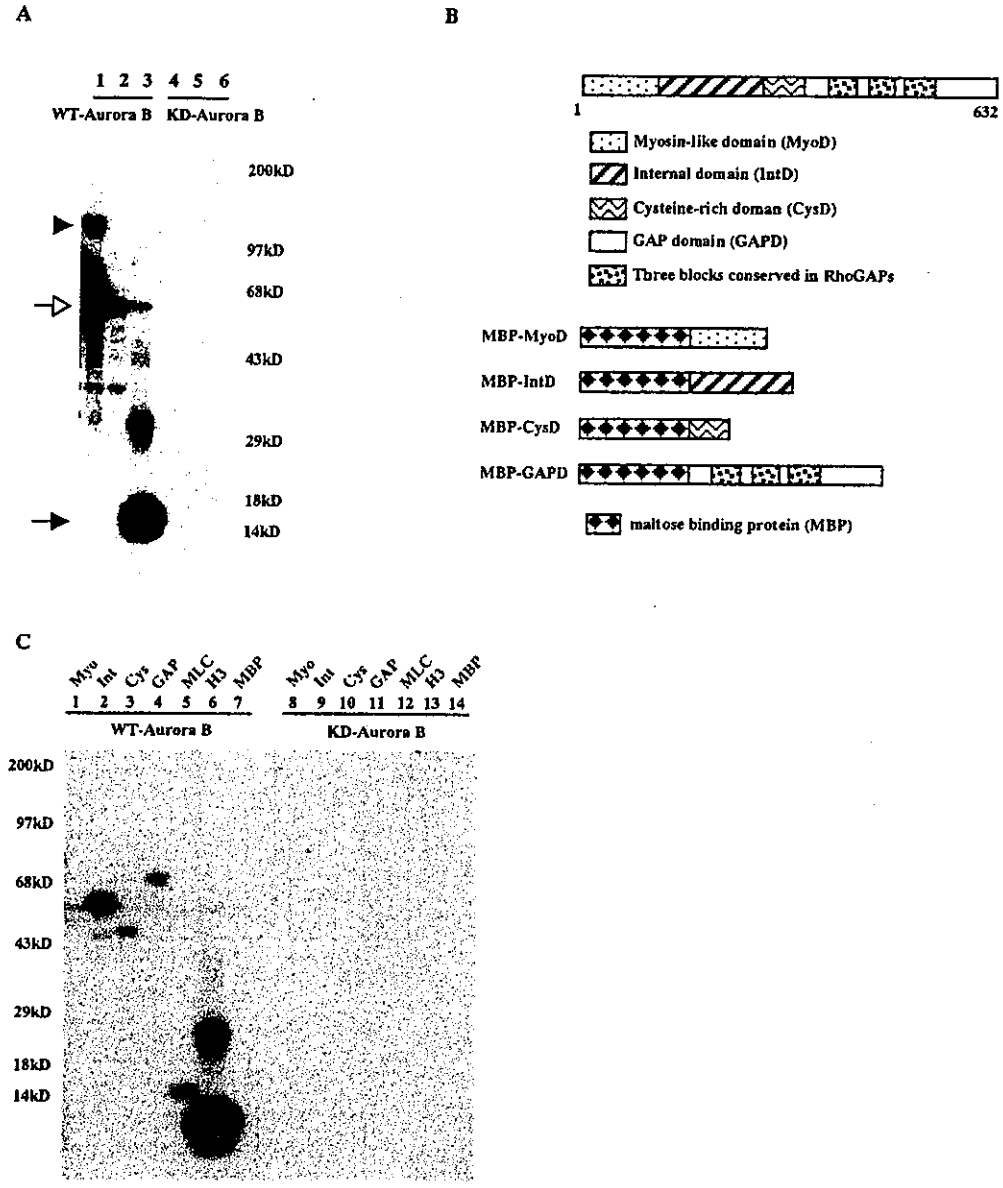

Figure 3. Aurora B Phosphorylates MgcRacGAP In Vitro

(A) Phosphorylation of MgcRacGAP is mediated by Aurora B in vitro. MBP-fused MgcRacGAP protein was incubated with the wild-type (WT) or a kinase-defective (KD) mutant of Aurora B. Histone H3 protein was used as a positive control. Histone H3 (lane 3, black arrow) and the MBP-fused full-length MgcRacGAP protein (lane 1, black arrowhead) were phosphorylated by the WT-Aurora B but not by the KD-Aurora B (lanes 4 and 6). No specific signal was detected on the 40 kDa of MBP protein used as a negative control by either the WT- or KD-Aurora B (lanes 2 and 5). Autophosphorylation of the WT-Aurora B fused to glutathione S-transferase (GST) is indicated by a white arrow.

(B) Structures of the full-length and MBP-fused derivatives of MgcRacGAP.

(C) In vitro kinase assay against MBP-fused derivatives of MgcRacGAP. Using the WT- or KD-Aurora B, MBP-fused derivatives of MgcRacGAP were incubated with the WT- or KD-Aurora B. Note that the *Int*, *Cys*, and *GAP* domains of MgcRacGAP but not the *Myo* domain were phosphorylated by the wild-type Aurora B. On the other hand, the KD-Aurora B did not induce phosphorylation of all the proteins tested. MBP and MLC stand for a negative control of MBP alone and myosin light chain, respectively.

of Rac1 protein was detected along the central spindle, distinct from that of MgcRacGAP (Figure 5, middle panels). On the other hand, at this stage of cytokinesis, RhoA clearly colocalized with MgcRacGAP, forming a ring-shaped structure around the midbody equator (Figure 5, upper panels). RhoA is known to promote contractile ring assembly by activating actin polymerization. Thus, immunostaining studies revealed that both RhoA